Time variation in igneous volume flux of the Hawaii-Emperor hot spot seamount chain

Emily Van Ark
Massachusetts Institute of Technology-Woods Hole Oceanographic Institution Joint Program, Cambridge, Massachusetts, USA

Jian Lin
Department of Geology and Geophysics, Woods Hole Oceanographic Institution, Woods Hole, Massachusetts, USA

Received 19 December 2003; revised 2 July 2004; accepted 5 August 2004; published 9 November 2004.

[1] Satellite gravity, ship track bathymetry, sediment thickness, and crustal magnetic age data were combined to calculate the residual bathymetry and residual mantle Bouguer gravity anomaly (RMBA) for the northwest Pacific Ocean. The Hawaii-Emperor hot spot track appears on the RMBA map as a chain of negative anomalies, implying thickened crust or less dense mantle. The hot spot swell is clearly visible in a broad band of half-width ~500 km for about 2000 km downstream from the current hot spot location, corresponding to hot spot ages of 0–25 Ma. A much narrower expression of the hot spot is visible for the rest of the chain at hot spot ages of 25–80 Ma. Comparison of the observed RMBA with various compensation models reveals that the relatively narrow features of the Hawaii-Emperor seamounts are best explained as being supported by plate flexure, while the Shatsky Rise, Hess Rise, and Mid-Pacific Mountains oceanic plateaus are best fit by Airy isostasy with a thickened crustal root. Amplitude comparisons between the RMBA predictions of various compensation models and the observed RMBA for the Hawaiian swell are ambiguous. However, on the basis of the shape of the predicted anomalies, we favor a model of flexure in response to a buried load at 120 km depth. We further calculate igneous (i.e., crustal) volume flux along the axis of the Hawaii-Emperor hot spot by integrating cross-sectional areas of gravity-derived excess crustal thickness and seafloor elevation, respectively, with respect to the normal oceanic crust. The highest values of the calculated igneous volume flux along the Hawaiian and Emperor ridges (~8 m^3/s) occur at present and at about 20 Ma. The flux was reduced to only 50% of this maximum (~4 m^3/s) at 10 Ma. The calculated igneous volume flux is systematically smaller (maximum values of ~4 m^3/s) along the Emperor ridge. Overall, the Hawaiian and Emperor ridges appear to have experienced quasi-periodic variations in fluxes on timescales of 6–30 Ma. Furthermore, during the low-flux periods at 25–48, 57, and 75 Ma the height and size of individual hot spot seamounts appear to be noticeably less than those of the high-flux periods. We hypothesize that the variations in the fluxes of the Hawaiian ridge might be controlled by the thickness of the overlying lithosphere at the time of hot spot emplacement, while the variations along the Emperor ridge may be influenced by the dynamics of the slow absolute motion of the hot spot at the time. *INDEX TERMS:* 3010 Marine Geology and Geophysics: Gravity; 3040 Marine Geology and Geophysics: Plate tectonics (8150, 8155, 8157, 8158); 8121 Tectonophysics: Dynamics, convection currents and mantle plumes; 9355 Information Related to Geographic Region: Pacific Ocean; 7220 Seismology: Oceanic crust; *KEYWORDS:* Hawaii-Emperor, hot spot, admittance, marine gravity, Northwest Pacific, igneous flux variability

Citation: Van Ark, E., and J. Lin (2004), Time variation in igneous volume flux of the Hawaii-Emperor hot spot seamount chain, *J. Geophys. Res.*, *109*, B11401, doi:10.1029/2003JB002949.

1. Introduction

[2] Hot spot plumes have often been imagined and modeled as stationary conduits of hot, enriched material from the deep mantle to the surface of the Earth [*Wilson*, 1963; *Morgan*, 1971; *Sleep*, 1990; *Schilling*, 1991; *Ribe and*

0148-0227/04/2003JB002949$09.00

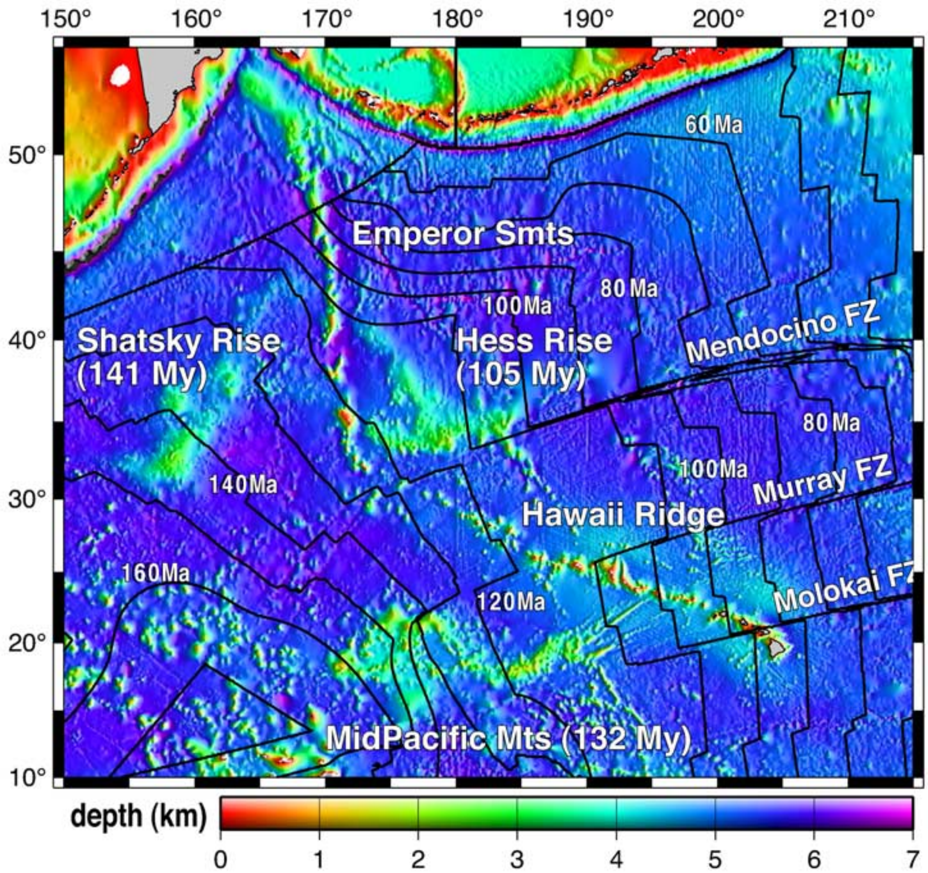

Figure 1. Interpolated ship track bathymetry showing the Hawaii-Emperor seamount chain, Hess and Shatsky Rises, and the Mid-Pacific Mountains. Also marked are the crustal age contours based on digital magnetic data of *Muller et al.* [1997] and the location of the Mendocino, Murray, and Molokai Fracture Zones.

Christensen, 1994; *Ito and Lin*, 1995; *Phipps Morgan et al.*, 1995; *Hoffman*, 1997; *Ribe and Christensen*, 1999; *Georgen et al.*, 2001]. This view is almost certainly too simplistic, but attempts at more complex models were limited by the scarcity of constraints on time variation in plume dynamics. Recent observations provide some of the constraints necessary for the development of time-varying models of hot spot behavior. One line of evidence uses new paleolatitudes found for several Emperor seamounts to calculate a southward drift rate of 30–50 mm/yr from 45–80 Ma for the Hawaii-Emperor hot spot [*Tarduno and Cottrell*, 1997; *Shipboard Scientific Party*, 2002a; *Cottrell and Tarduno*, 2003; *Tarduno et al.*, 2003]. New models of mantle convection incorporating stratified mantle viscosities and rigid plates show the natural evolution of dynamic plume systems alternating between periods of motion and periods of relative stability [*King et al.*, 2002; *Lowman et al.*, 2003]. This study attempts to quantify variations in the Hawaiian plume igneous (crustal) production over time.

[3] A number of approaches have been proposed to estimate fluxes of hot spot material. These have generally fallen into three categories: estimates of the buoyancy or mass flux of the hot spot's underlying mantle plume, estimates of the volume flux of the underlying mantle plume, and estimates of the igneous volume flux produced by hot spot melting. Buoyancy flux estimates generally assume isostatic compensation of the hot spot swell, the broad topographic anomaly associated with a hot spot. The rate at which the swell is generated can then be used to estimate the buoyancy or mass flux of the underlying mantle plume [*Davies*, 1988, 1992; *Sleep*, 1990]. Volume fluxes of hot spot mantle plumes have been estimated using fluid dynamics models [*Sleep*, 1990; *Ribe and Christensen*, 1994] and geochemical signatures of plume interactions with mid-ocean ridges [*Schilling*, 1991].

[4] Volcanic or igneous fluxes of the Hawaii-Emperor hot spot have been estimated by several authors using bathymetry data alone. *Bargar and Jackson* [1974] were the first to calculate the volume of individual volcanic shields along the Hawaii-Emperor chain, resulting in values ranging from 42.5×10^3 km^3 for Mauna Loa to 0.3×10^3 km^3 for a shield on one of the northernmost Emperor seamounts. *White* [1993] assumed Airy isostasy supporting observed bathymetry to estimate the total melt production of the Hawaii-Emperor chain over time, arriving at values of 0.03–0.16 km^3/yr (or 0.95–5.08 m^3/s). Most recently, *Vidal and Bonneville* [2004] used bathymetry with Airy isostasy and flexure assumptions to calcu-

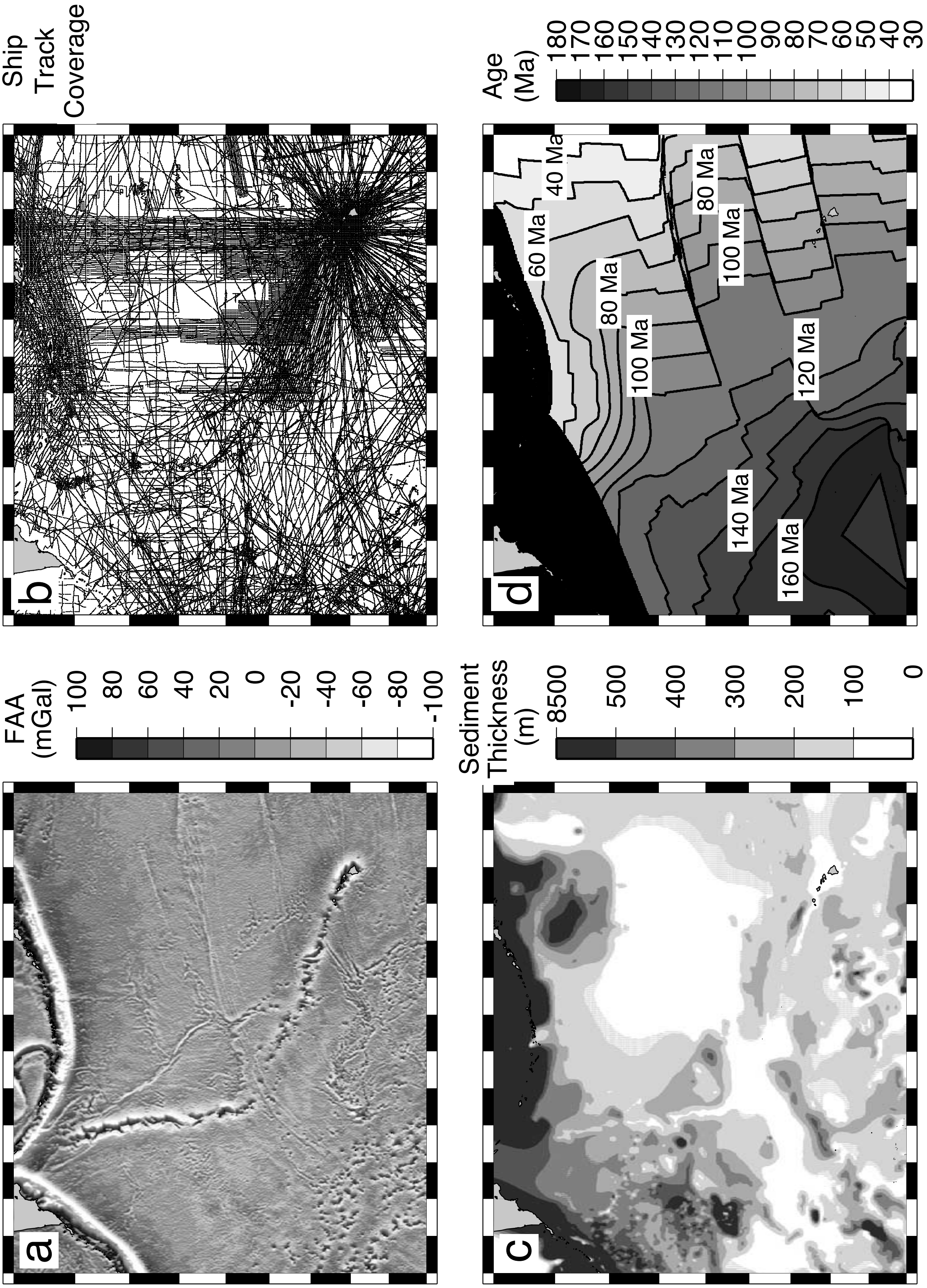
a
FAA (mGal)
100
80
60
40
20
0
-20
-40
-60
-80
-100
b
Ship Track Coverage
c
Sediment Thickness (m)
8500
500
400
300
200
100
0
d
Age (Ma)
180
170
160
150
140
130
120
110
100
90
80
70
60
50
40
30
40 Ma
60 Ma
80 Ma
100 Ma
120 Ma
140 Ma
160 Ma
150°
160°
170°
180°
190°
200°
210°
50°
40°
30°
20°
10°

Figure 2

late magma production rates for Hawaii in a continuous manner. Our method is similar to that of *Vidal and Bonneville* [2004] in that it produces a continuous along-axis volcanic flux measurement. However, in addition to using bathymetry data, we also use gravity anomalies to constrain crustal thickness.

[5] This paper uses satellite gravity anomalies and shipboard data to show that the igneous crustal production of the Hawaii-Emperor hot spot has changed over the history of the hot spot on timescales of 6–30 My, with the igneous volume flux varying between 0 and 10 m^3/s. We have chosen to study the Hawaii-Emperor hot spot because it has the longest and clearest hot spot track on Earth, and therefore offers the longest time record of possible hot spot flux variations. Unlike many other hot spots, the Hawaii-Emperor track is not complicated by complex interactions with mid-ocean ridges. We also compare the observed residual gravity anomaly with different models of isostatic compensation to investigate the specific geodynamic mechanisms supporting the topography of the relatively narrow Hawaiian-Emperor seamounts, the broad Hawaiian swell, and the Mid-Pacific Mountains, Hess Rise, and Shatsky Rise oceanic plateaus.

2. Data

[6] Our study utilizes four global data sets: satellite free air gravity [*Sandwell and Smith*, 1995, 1997], oceanic sediment thickness [*Divins*, 2001], ship track bathymetry [*Smith and Sandwell*, 1994, 1997], and oceanic crustal age [*Muller et al.*, 1997]. From each of these data sets we select a study region of 150°E to 215°E and 10°N to 55°N in the northern Pacific Ocean (Figure 1).

[7] The satellite marine free air gravity map of *Sandwell and Smith* [1995, 1997] (Figure 2a) is available as a 1 min by 1 min database that was derived from satellite altimetry taken on the Geosat and ERS1 missions. The Hawaii-Emperor seamount chain is a prominent feature on this map due to the point-like, uncompensated loading of the seamounts on the plate. In contrast, longer wavelength areas of crustal thickening are isostatically compensated by deformation of the elastic plate and/or crustal underplating and are therefore not prominent on the free air gravity map. Because this is a marine gravity data set, we lack coverage for the Hawaiian islands. We have therefore masked out the Hawaiian islands on all our calculation results presented as maps. This lack of Hawaiian island coverage results in an underestimation of the igneous volume flux at the current hot spot position, but does not limit our ability to quantify the long-period variation of the Hawaiian hot spot flux over time.

[8] Global ship track bathymetry has been compiled by the National Geophysical Data Center (NGDC) and is available on CD. The same information has been incorporated into the *Smith and Sandwell* [1994, 1997] predicted topography map along with data from various other archives. The ship track coverage of the Hawaii-Emperor seamount chain and its surrounding region is adequate for our purposes (Figure 2b). Prominent tectonic features in our study region include the Hawaii-Emperor seamount chain, the Mid-Pacific Mountains (MPM), Shatsky Rise, and Hess Rise (Figure 1). Ocean Drilling Program results dated the sediments on the MPM to be at least 123–132 Ma old [*Arnaud-Vanneau and Sliter*, 1995; *Jenkyns*, 1995; *Jenkyns et al.*, 1995; *Pringle and Duncan*, 1995] and paleomagnetic studies of basalts from the MPM [*Tarduno and Sager*, 1995] support the interpretation of its formation over the region of thinned, weak lithosphere and low-viscosity asthenosphere bathymetrically expressed as the Pacific Superswell [*McNutt and Judge*, 1990]. The formation of Hess Rise, to the northeast of the bend in the Hawaii-Emperor chain, has been dated at 98–110 Ma [*Pringle and Dalrymple*, 1993] and is thought to have formed on or very near the Pacific-Farallon spreading center [*Vallier et al.*, 1981; *Kroenke and Nemoto*, 1982; *Mammerickx and Sharman*, 1988]. Shatsky Rise, to the west of the bend in the hot spot track, has been dated at 138–145 Ma [*Sager and Han*, 1993; *Shipboard Scientific Party*, 2002b] and magnetic lineations around the rise indicate that it formed along the trace of the Pacific-Farallon-Izanagi triple junction [*Larson and Chase*, 1972; *Hilde et al.*, 1976; *Sager et al.*, 1988; *Nakanishi et al.*, 1989, 1999]. The bend in the hot spot track has been dated between 40 and 53 Ma [*Sharp and Clague*, 2002] and its origin is interpreted to be related to the cessation of southward motion of the Hawaii-Emperor hot spot that has been measured for the Emperor segment of the seamount chain [*Tarduno and Cottrell*, 1997; *Shipboard Scientific Party*, 2002a; *Cottrell and Tarduno*, 2003; *Tarduno et al.*, 2003].

[9] The oceanic sediment thicknesses map of *Divins* [2001] was compiled from three primary sources: previously published isopach maps [*Divins and Rabinowitz*, 1991; *Hayes and LaBrecque*, 1991; D. L. Divins and B. Eakins, manuscript in preparation, 2004], DSDP and ODP ocean drilling results, and seismic reflection and refraction data archived by the National Geophysical Data Center (NGDC) and the Intergovernmental Oceanographic Commission (IOC) Geological/Geophysical Atlas of the Pacific (GAPA) project. The possible influence of strongly reflective chert and volcanic layers above the acoustic basement lead to seismic estimates of sediment thickness that represent a minimum value. The average background thickness over most of the northwest Pacific is 100 m, although much

Figure 2. Data used to calculate the northwest Pacific gravity anomalies. (a) Free air gravity anomaly from satellite altimetry [*Sandwell and Smith*, 1997]. The Hawaii-Emperor seamount chain is clearly visible, with positive anomalies of up to 200 mGal due to the lack of compensation of these short-wavelength features. The broad Hawaiian swell is marginally visible. Other major bathymetric features of the region such as the Hess and Shatsky Rises and the Mid-Pacific Mountains do not appear as prominent features on the free air anomaly map, indicating probable shallow isostatic compensation. (b) Ship track bathymetry coverage from the National Geophysical Data Center and *Smith and Sandwell* [1994, 1997]. (c) Marine sediment thickness map for the northwest Pacific [*Divins*, 2001]. (d) Oceanic crustal age based on the digital magnetic data of *Muller et al.* [1997].

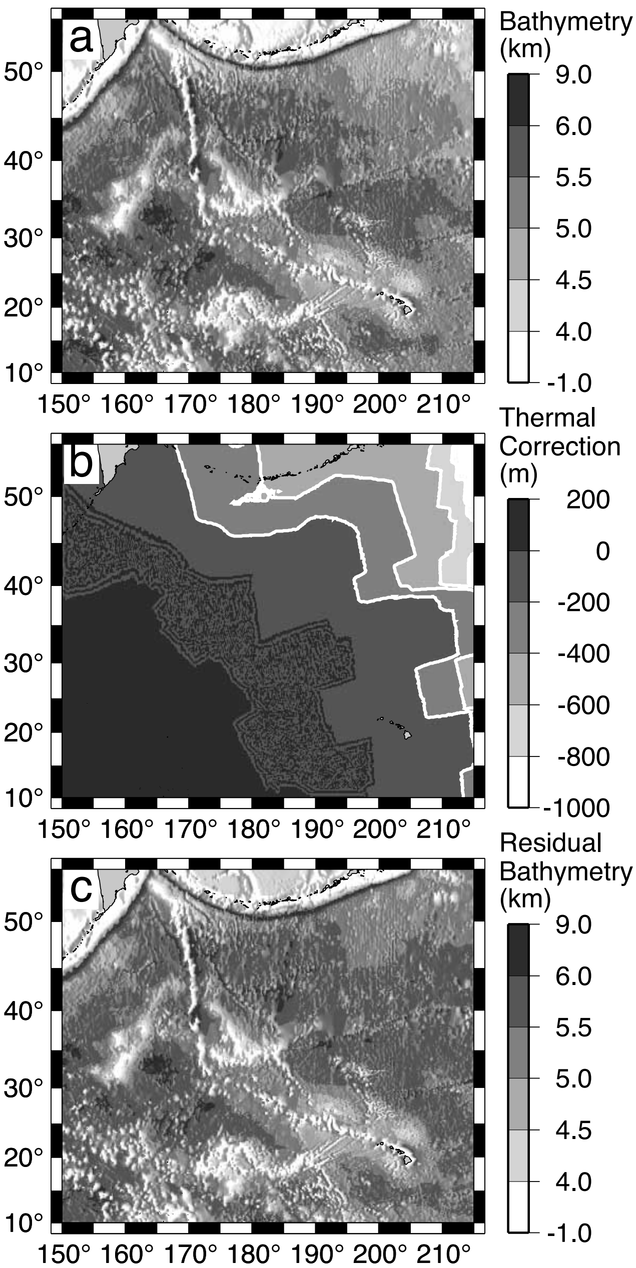

Figure 3. Residual bathymetry calculation. (a) Ship track bathymetry. (b) Thermal bathymetric correction calculated from the plate cooling model as discussed in the text. (c) Residual bathymetry calculated by subtracting thermal bathymetric correction in Figure 3b from the ship track bathymetry in Figure 3a.

greater values are reached near the continental margins (Figure 2c).

[10] The *Muller et al.* [1997] digital age grid of the ocean floor (Figure 2d) has a grid spacing of 6 min. It was created from a compiled global magnetic database and models of global plate reconstruction. Ten million year age contours overlain on the northwest Pacific bathymetry map (Figure 1) reveals that the Hawaii seamounts were emplaced on crust that was, on average, 70–80 My old at the time of active volcanism. We also note that the Hawaii-Emperor chain crosses, from northwest to southeast, the Mendocino, Murray, and Molokai Fracture Zones (Figure 1).

3. Analysis and Results

3.1. Residual Bathymetry

[11] We calculate residual bathymetry by correcting observed ship track bathymetry for the effect of plate cooling. This calculation is done in three steps. First the three-dimensional thermal structure of the Pacific lithosphere is calculated at each grid point from 0 to 100 km depth using the digital age grid and a simple plate cooling model [*Turcotte and Schubert*, 2002] with thermal diffusivity $\kappa = 10^{-6}$ m^2/s. We used temperature boundary values of $T_0 = 0°$C at the surface of the plate and $T_1 = 1350°$C at a plate thickness of $z_{L0} = 100$ km, which are parameters chosen as intermediate values between the plate models of *Parsons and Sclater* [1977] and *Stein and Stein* [1992].

[12] The thermal structure is next translated into a density anomaly structure using a simple thermal expansion equation, $\Delta\rho = (T_0 - T)\alpha\rho_0$, where T_0 and ρ_0 represent reference temperature and density, respectively, and α is the coefficient of thermal expansion. We used $\rho_0 = 3300$ kg m^{-3} and $\alpha = 3.4 \times 10^{-5}$ K^{-1} with the reference temperature T_0 set equal to the value in the middle of our study region. We are therefore calculating an anomaly relative to center of our map, so that areas with temperatures higher than the center of our map will have a negative density anomaly while areas with temperatures lower than the center of our map will have a positive density anomaly.

[13] Finally, the density anomalies of the thermal model are translated into expected topography, h, based on a simple isostatic model: $h(x, y) = [1/(\rho_m - \rho_w)] \int_0^{zL0} \Delta\rho \, dz$, where ρ_m and ρ_w are the average densities of the mantle and the ocean water, respectively. Since the thermal density anomaly $\Delta\rho$ may be positive or negative relative to the value at the center of our map, the resulting expected topography may be positive or negative relative to that reference value. The calculated thermal topography (Figure 3b) is subtracted from the actual bathymetry (Figure 3a) to produce the residual bathymetry (Figure 3c). This correction deepens the youngest lithosphere (~30 Ma) relative to the mean bathymetry, reducing the range between the shallowest and deepest bathymetry by ~1 km in the resultant residual bathymetry (Figure 3).

3.2. Gravity Anomalies

[14] Gravity anomalies are used to investigate subseafloor density variations. The Bouguer anomaly (BA) is found by subtracting the attraction of sediment cover and seafloor topography from the free air anomaly, while the mantle Bouguer anomaly (MBA) subtracts the additional attraction of the crust-mantle interface assuming an average 6-km-thick uniform crust. The residual mantle Bouguer anomaly (RMBA), similar to the residual bathymetry discussed above, further subtracts out the gravitational influence of plate cooling using the same three-dimensional thermal model as in the residual bathymetry calculations. The resultant RMBA should reflect variations in crustal density and thickness, or variations in mantle density, or both. We calculate MBA and RMBA using an upward continuation

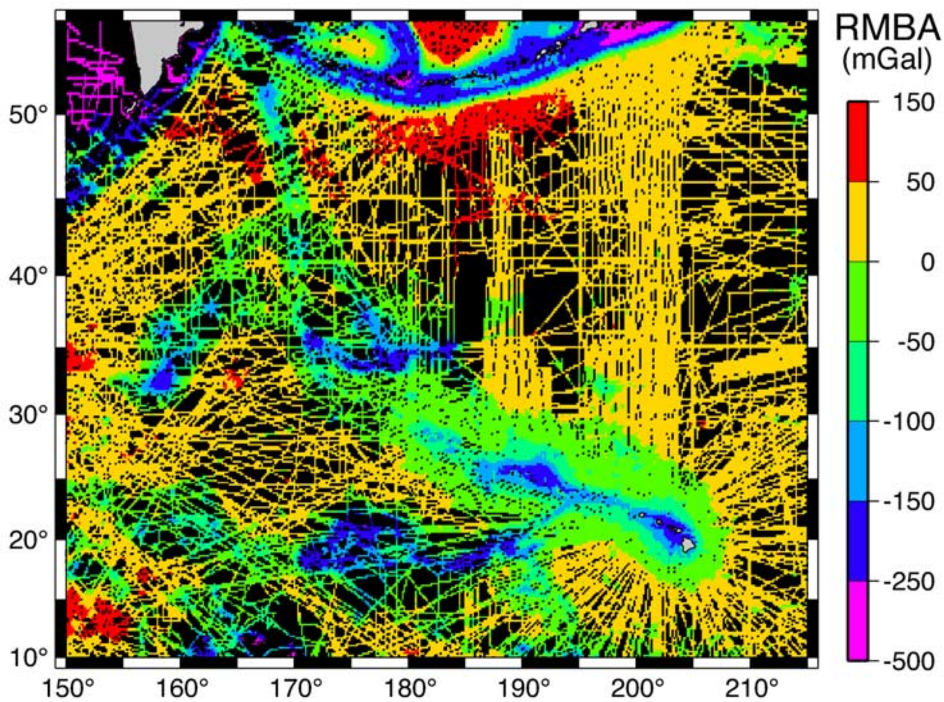

Figure 4. Residual mantle Bouguer anomaly for the northwest Pacific region. Prominent negative anomalies are seen for the Hawaii-Emperor seamount chain, the Hawaiian hot spot swell, the Hess and Shatsky Rises, and the Mid-Pacific Mountains (see location of these features in Figure 1).

algorithm developed by *Parker* [1972] and implemented by *Kuo and Forsyth* [1988].

[15] The effect of the Hawaii-Emperor hot spot on the northwest Pacific lithosphere is clearly visible as a broad region of negative RMBA anomalies coinciding with the seamounts and swell of the hot spot chain (Figure 4). The magnitude of Hawaii-Emperor hot spot RMBA anomalies reaches −200 mGal, larger than any other hot spot except Iceland (up to −300 mGal) [*Ito et al.*, 1996]. The swell anomaly is ~1000 km wide and extends upstream for ~2000 km. The Hess and Shatsky Rises as well as the Mid-Pacific Mountains are also prominent features on the RMBA map (Figure 4), in comparison to their smaller signal on the free air gravity anomaly map.

3.3. Admittance

[16] Admittance functions predict the gravity anomaly associated with a given surface topography for specified assumptions about how the topographic load is supported [*Watts*, 2001]. Admittance functions were earlier applied to understanding the relationship between free air gravity anomalies and elevations of the Hawaii-Emperor seamounts by *Watts* [1978]. Following the approach of *Ito and Lin* [1995], we investigate admittance functions for the northwest Pacific to better understand the sources of our calculated mantle Bouguer gravity anomalies. A generic gravitational admittance function $Z(k)$ is defined as

$$\Delta g(\mathbf{k}) = Z(k)H(\mathbf{k}), \tag{1}$$

where $\mathbf{k}$ is the two-dimensional wave number, $k = |\mathbf{k}| = 2\pi/\lambda$, $\Delta g(\mathbf{k})$ is the Fourier transform of the gravity anomaly and $H(\mathbf{k})$ is the Fourier transform of the topography of an interface such as the seafloor or Moho. We test admittance functions for Airy isostasy, surface load plate flexure with a range of elastic plate thicknesses, and buried load plate flexure with a range of load depths. Each of these functions is applied to the northwest Pacific residual bathymetry to calculate a corresponding map of predicted RMBA. These predicted RMBA maps are then compared with the observed RMBA to assess which mechanisms of isostatic compensation can best explain each of the major bathymetric features in the northwest Pacific. This comparison is quantified by calculating the root mean square (rms) of the misfit between the admittance-predicted RMBA and the observed RMBA over the areas of interest outlined in Figure 5. The results of the comparison are presented in Figure 6 and parameters used in admittance functions are given in Table 1.

3.3.1. Airy Isostasy

[17] Airy isostasy is a model in which the lateral variations in surface topography are assumed to be supported by subsurface variations in the thickness of the crust. The free air gravity anomaly for Airy isostasy would therefore have contributions from the seafloor and crustal-mantle interfaces. When calculating the mantle Bouguer anomaly and RMBA, we have subtracted the gravitational effects of the seafloor interface and an assumed reference crust that follows the bathymetry. The RMBA admittance function for Airy compensation of residual bathymetry is therefore given by

$$Z(k)_{\mathrm{Airy}} = -2\pi G[(\rho_m - \rho_c)\exp(-kz_{\mathrm{RM}}) + (\rho_c - \rho_w)\exp(-kz_{\mathrm{CR}})], \tag{2}$$

where ρ_w, ρ_c, and ρ_m are the densities of the seawater, crust, and mantle respectively, z_{RM} is the reference Moho depth below sea level, and z_{CR} is the assumed mean depth of the crustal root below sea level [*Ito and Lin*, 1995]. The first term of this expression subtracts the attraction of the reference crust and the second term reflects the attraction of the crustal root assumed to support the overlying topography.

[18] We use 11 km for z_{RM} since the mean ocean depth in the Pacific is ~5 km and our reference Moho is 6 km below the seafloor. We use 17 km for z_{CR} as this seems consistent with the seismic result available for the Hawaiian islands [*ten Brink and Brocher*, 1987]. The results from applying $Z(k)_{Airy}$ to the residual bathymetry (Figures 5b and 5c) show a good match to the observed RMBA for the Hess and Shatsky Rises and the Mid-Pacific

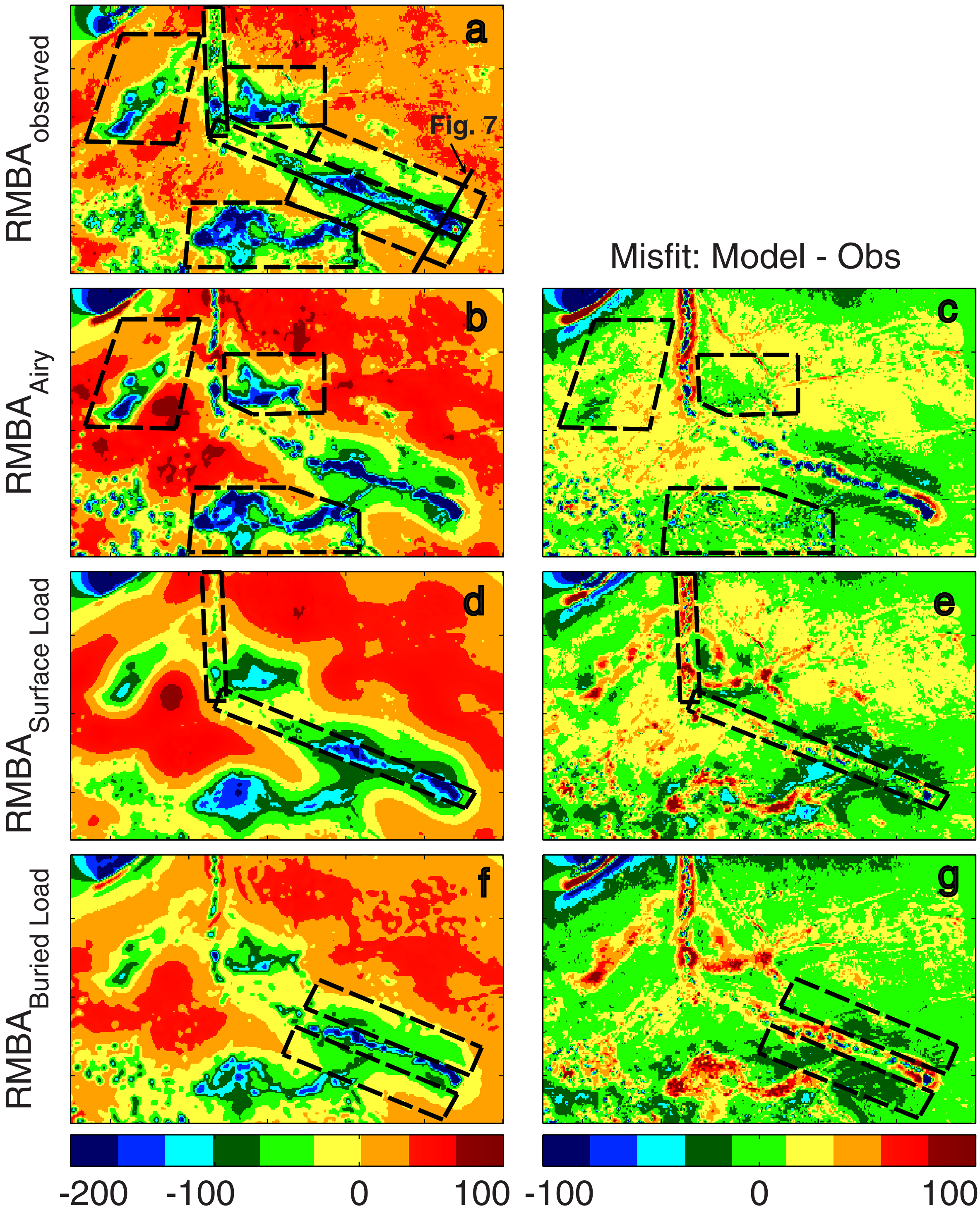

Figure 5

Mountains. However, Airy isostasy does less well predicting the RMBA signature of the Hawaiian swell and greatly overpredicts the negative RMBA associated with short wavelength signals such as the Hawaii-Emperor seamount chain (Figure 6).

3.3.2. Plate Flexure With Surface Loading

[19] Elastic plate flexure models predict bending of a plate under applied loads. In this section we examine flexure models associated with topography loads applied on the surface of the elastic plate. This results in crustal deflection similar to the Airy model, but the deflection is dependent on the wavelength of the load and is distributed over a broader region. The RMBA admittance function for flexure with surface loading is therefore given by

$$Z(k)_{\text{Surface Load}} = -2\pi G[(\rho_m - \rho_c)\exp(-kz_{\text{RM}}) + (\rho_c - \rho_w)\exp(-kz_{CR})\phi'_e(k)], \quad (3)$$

which is very similar in form to $Z(k)_{\text{Airy}}$ except that the crustal root term now has an additional multiplication factor $\phi'_e(k)$, which is defined as

$$\phi'_e(k) = \left[\frac{Dk^4}{(\rho_m - r_c)g} + 1\right]^{-1}, \quad (4)$$

where g is the acceleration of gravity, $D = Eh_e^3/12(1 - \nu^2)$ is the flexural rigidity of the plate, E is Young's modulus, h_e is the elastic thickness of the plate, and ν is Poisson's ratio [*Watts*, 2001]. Previous studies of flexure of the lithosphere under the Emperor and Hawaiian seamounts have suggested values for h_e between 10.5 and 40 km, depending on the location of the study along the seamount chain and the method used [*Walcott*, 1970; *Watts and Cochran*, 1974; *Watts*, 1978; *Kunze*, 1980; *Watts et al.*, 1985; *Calmant*, 1987]. We apply $Z(k)_{\text{Surface Load}}$ to the residual bathymetry using the parameters of Table 1, including a range of elastic plate thicknesses: 20, 30, 40, 50, 60, 70 and 80 km.

[20] Comparison of the observed RMBA with the RMBA predicted from $Z(k)_{\text{Surface Load}}$ (Figures 5d and 5e) reveals that the flexure equation with surface loading does better in predicting the gravity anomalies from the relatively narrow Hawaiian and Emperor seamounts than other forms of compensation, although plate flexure with buried loading at a depth of 150 km (presented in the next section) also has a relatively low rms misfit for the Hawaiian seamounts (Figure 6). For the surface loading flexure models, the Hawaiian seamounts are better fit with thicker elastic thicknesses, 60 km, while the Emperor seamounts are better fit with thinner elastic thicknesses, 30 km (Figure 6). In contrast, the flexure model with surface loading does not do as well as the Airy model in predicting the gravity signature of the Hess, Shatsky, and Mid-Pacific igneous plateaus. The surface loading flexure model produces a relatively small rms misfit for the Hawaiian swell (Figure 6).

3.3.3. Plate Flexure With Buried Loading

[21] The final option we consider for supporting seafloor topography is a buried load exerting forces on an interface below the crust. This is essentially plate flexure with the load exerted by a buried density anomaly at the bottom of the elastic plate. In such a case, the surface topography H(k) is a function of the interface between the underlying load and the normal mantle, $W(k)$:

$$H(k) = -W(k)\frac{(\rho_m - \rho_L)}{(\rho_m - \rho_w)}\phi''_e(k), \quad (5)$$

where ρ_L is the density of the load, ϕ''_e is defined as

$$\phi''_e(k) = \left[\frac{Dk^4}{(\rho_m - \rho_w)g} + 1\right]^{-1}, \quad (6)$$

and D has the same definition as in the surface load flexure model [*Watts*, 2001]. After we rearrange equation (5) so that $W(k)$ is in terms of $H(k)$, we find that the admittance equation for a buried load is

$$Z(k)_{\text{Buried Load}} = -2\text{p}G(\rho_m - \rho_w)\frac{\exp(-kz_L)}{\phi''_e(k)}, \quad (7)$$

where z_L is the depth of the buried load supporting the topography. There is only one term in equation (7) because the lack of crustal thickening in this model enables the mantle Bouguer corrections to eliminate all the crustal interfaces. The presence of the flexural rigidity, D, in equation (6) results in the inclusion of the elastic plate thickness h_e in this set of admittance models as well as the flexure models above. Rather than run every buried load model with a range of h_e values, we use a value of 40 km which is intermediate between the two values which best fit the Hawaiian and Emperor seamounts in our calculations and is consistent with previous estimates of h_e for the Hawaii-Emperor system (catalogued by *Watts and Zhong* [2000]).

Figure 5. Admittance model comparisons. (a) "Observed RMBA" calculated from ship track bathymetry and satellite free air gravity anomalies. The areas used to calculate the rms misfit between the admittance predictions and the observed gravity anomalies are outlined with dashed boxes. The line across the Hawaiian seamounts and swell is the profile used for Figure 7. All values are in mGal. (b) RMBA predicted by Airy isostatic compensation of bathymetry. (c) Misfit between the RMBA modeled with Airy isostasy and the observed RMBA. The areas contained in the dashed boxes (the Mid-Pacific Mountains, Shatsky Rise, and Hess Rise) are well modeled by Airy isostasy and have a small misfit. (d) RMBA predicted from elastic plate flexure under the observed bathymetric load with an effective elastic thickness of 60 km. (e) Misfit between the surface loading flexure model of RMBA and the observed RMBA. In general, the surface loading flexure equation best predicts the gravity anomalies in the dashed boxes containing the Hawaii and Emperor seamounts. (f) RMBA predicted from a buried load plate flexure admittance function with an elastic plate thickness of 40 km and a load depth of 120 km. (g) Misfit between the buried load model of RMBA and the observed RMBA. The buried load model best predicts the shape of the gravitational anomaly due to the Hawaiian swell contained within the dashed boxes.

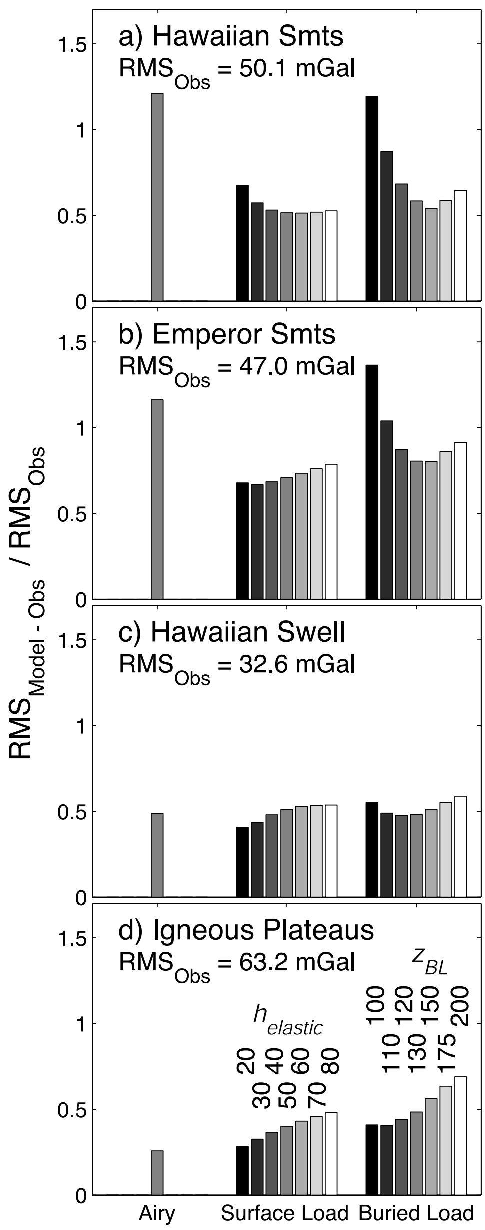

Figure 6. Comparison of misfit between admittance models with varying model parameters and the observed RMBA for selected bathymetric features of the northwest Pacific: (a) the Hawaiian ridge seamounts; (b) the Emperor seamounts; (c) the Hawaiian swell; and (d) the large igneous plateaus of the region (Hess and Shatsky Rises and the Mid-Pacific Mountains). The rms values of the model minus the observed RMBA misfit for each region has been normalized by the rms of the observed RMBA in that region. The regions chosen for evaluation of the rms misfit are shown as dashed boxes in Figure 5. The bars for the elastic plate flexure model represent different values of elastic plate thickness (from left to right, 20, 30, 40, 50, 60, 70, and 80 km). The bars for the buried load model represent different values of load depth (from left to right, 100, 110, 120, 130, 150, 175, and 200 km).

[22] Previous studies of subsurface support of the Hawaiian swell have found loading or compensation depths of 100–200 km [*Watts*, 1976], 70–120 km [*Crough*, 1978], 40 km [*Sandwell*, 1982], and 70 km [*McNutt and Shure*, 1986]. We apply $Z(k)_{\mathrm{Buried\ Load}}$ to the residual bathymetry for z_L = 100, 110, 120, 130, 150, 175, and 200 km. Comparing the observed RMBA with the RMBA predicted from $Z(k)_{\mathrm{Buried\ Load}}$ (Figure 5f and 5g) reveals that while the buried load flexure model does a poor job of predicting the gravity anomaly for the seamounts and the igneous plateaus, it does noticeably better at predicting the gravitational signal for the Hawaiian swell with the best fit model obtained for a load depth of z_L = 120 km (Figure 6). As noted above, the surface load flexure admittance model also produces relatively small rms values for the Hawaiian swell region. However, the buried load more closely models the spatial shape of the anomaly for the swell (Figures 5 and 7).

3.3.4. Admittance Comparison

[23] By focusing in on key portions of our study area (Figures 5 and 6) we can compare in detail the results of the above three models of topography support. While it is simplistic to assume that any one mechanism completely accounts for the support of complicated tectonic features such as the Hawaiian ridge and swell system, attempting to separate out the fractional contribution of each mechanism to every major feature is a problem of complexity beyond the scope of this paper. However, by geographically separating out individual regions, we can attempt to constrain the dominant mechanism for those regions of interest. Separating out the Hawaiian and Emperor seamount chains from the Hawaiian swell and igneous plateaus has the additional benefit of providing a sort of ad hoc wavelength separation.

[24] The smallest rms misfit between the observed RMBA and the RMBA predicted by our admittance models for the Hawaiian swell is given by flexure due to surface loading with an elastic plate thickness of 20 km. However, comparison of the results for the swell in Figures 5 and 7 reveals that the shape of the swell is better eliminated from the misfit by the buried load flexure model with a load depth of 120 km. Thus while the results of the modeling are inconclusive, we prefer the interpretation that the swell is supported by a buried load at 120 km depth, which is consistent with the common attribution of the swell to low-density (either hot or chemically depleted) hot spot material trapped beneath the lithosphere at a depth found in previous studies to be between 40 and 200 km [*Watts*, 1976; *Crough*, 1978; *Sandwell*, 1982; *McNutt and Shure*, 1986; *Phipps Morgan et al.*, 1995]. Our interpretation is also compatible with the recent discovery of 100–110 km thick lithosphere under the island of Hawaii with lithospheric thinning to 50–60 km upstream under the island of Kauai by *Li et al.* [2004] using *S* wave receiver functions. Likewise, the low-velocity *P* wave seismic anomaly observed in the shallow mantle under the Hawaiian swell region by *Montelli et al.* [2004] is consistent with a buoyancy anomaly supporting the swell. Finally, multichannel seismic data collected by *ten Brink and Brocher* [1988] shows normal crustal thickness values of 6–7 km in areas of the Hawaiian swell north and south of Oahu, further supporting the interpretation of deep mantle support for the swell

Table 1. Parameters Used in Admittance Calculations and Associated Functions

Variable	Symbol	Value	Function(s)[a]
Ocean water density, kg/m^3	ρ_w	1030	airy, surface, buried
Crustal density, kg/m^3	ρ_c	2800	airy, surface
Mantle density, kg/m^3	ρ_m	3300	airy, surface, buried
Reference Moho depth from sea surface, km	z_{RM}	11	airy, surface
Crustal root depth from sea surface, km	z_{CR}	17	airy, surface
Depth of buried load from sea surface, km	z_L	100, 110, 120, 130, 150, 175, and 200	buried
Thickness of elastic plate, km	h_e	20, 30, 40, 50, 60, 70, and 80	surface, buried
Young's modulus, Pa	E	7×10^7	surface, buried
Poisson's ratio	ν	0.25	surface, buried
Gravitational constant, m^3/(kgs^2)	G	6.67×10^{-11}	airy, surface, buried
Gravity acceleration, m/s^2	g	9.8	surface, buried

[a]"Surface" and "buried" indicate that use in the equations associated the surface load plate flexure and buried load plate flexure, respectively.

topographic anomaly rather than the shallow crustal support which would be implied by plate flexure with surface loading.

[25] In contrast, the RMBA of the Hawaiian and Emperor seamounts are best modeled in our results by surface load flexure with 60 and 30 km elastic plate thicknesses, respectively. Although the rms misfit for the 150 km deep buried load flexure model is almost as small as the best surface load flexure models for the Hawaiian seamounts, a close examination of Figures 5e and 5g reveals that the surface loading flexure model does a better job of modeling the shape of the flexural moat associated with the seamounts. The success of the surface loaded flexural admittance model is perhaps to be expected as such short-wavelength features are commonly understood to be supported by plate strength. Previous studies have found greater elastic thicknesses for the Hawaiian islands and the Hawaiian ridge than for the Emperor Seamounts [*Walcott*, 1970; *Watts and Cochran*, 1974; *Watts*, 1978; *Kunze*, 1980; *Watts et al.*, 1985; *Calmant*, 1987; *Watts and Zhong*, 2000]. *Watts and Zhong* [2000] suggest that the apparent elastic thickness of a plate increases with the thermal age of the plate at the time of loading and decreases with time after loading due to the viscoelastic behavior of the plate. Both of these factors could explain the smaller elastic plate thickness estimates for the Emperor seamounts, which were emplaced much earlier and on younger lithosphere [*Mammerickx and Sharman*, 1988; *Keller et al.*, 2000]. While our estimate agrees with that trend, the magnitude of our values is greater than most of those studies. This may be in some measure due to the fact that we are using a two-dimensional admittance function and averaging over the entire Hawaiian and Emperor seamount chains, while previous studies have looked at discrete cross-axis profiles along the chains. Additionally, it is important to note that the swell does not cease to exist under the seamounts and therefore the gravitational anomaly we measure probably has contributions from both surface loading of the seamounts and the buried load that supports the swell.

[26] Lastly, the Mid-Pacific Mountains, Hess Rise, and Shatsky Rise are best modeled by Airy isostasy. Figure 5c shows that Hess and Shatsky are extremely well modeled at all wavelengths, while the larger wavelengths of the Mid-Pacific Mountains are well modeled but the small wavelength features remain uncompensated. This is consistent with an interpretation of the Mid-Pacific Mountains, Hess Rise, and Shatsky Rise as old igneous plateaus that were emplaced on young, weak lithosphere at spreading centers (Hess and Shatsky Rises) or over low-viscosity mantle (Mid-Pacific Mountains) that has relaxed to the point where the load floats in isostatic equilibrium. The Mid-Pacific Mountains, Hess Rise, and Shatsky Rise are

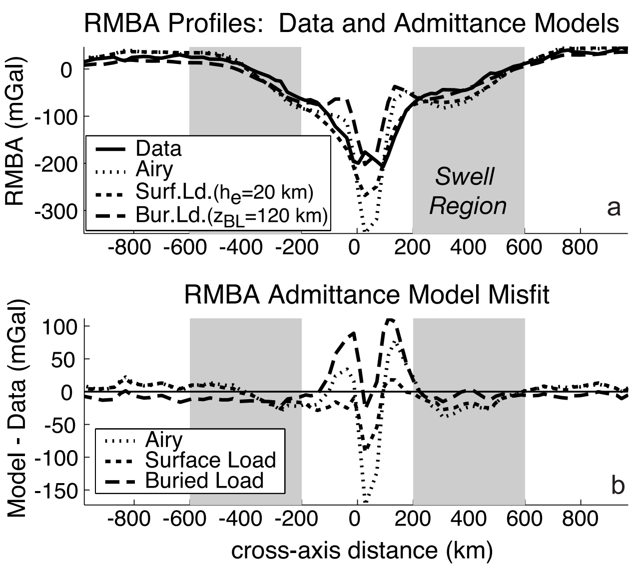

Figure 7. (a) Profiles of the "observed" RMBA calculated from the free air gravity anomaly and the modeled RMBA calculated from topography using admittance functions for Airy isostasy, flexure of a thin elastic plate of thickness 20 km, and flexure of an elastic plate of thickness 40 km in response to a buried load at 120 km depth. (b) Misfit between the modeled RMBA amplitudes and the observed amplitudes for each of the admittance models along the same profile. The profile used is shown in Figure 5a, and the shaded regions on the profiles show the region used to calculate the Hawaiian swell misfit. It can be seen that while the amplitudes of the misfits for Airy and flexure admittance are comparable to that of the buried load, the buried load has a much flatter misfit function. This indicates that the buried load at 120 km better models the shape of the Hawaiian swell and in turn makes this our preferred model for the support of the Hawaiian swell.

dated as old as 123–132 Ma [*Arnaud-Vanneau and Sliter*, 1995; *Jenkyns*, 1995; *Jenkyns et al.*, 1995; *Pringle and Duncan*, 1995], 98–100 Ma [*Pringle and Dalrymple*, 1993], and 138–145 Ma [*Sager and Han*, 1993; *Shipboard Scientific Party*, 2002b], respectively. Recent two-layer viscoelastic models of the lithosphere show that for cases where the viscosity ratio between the upper and lower layers is on the order of $10^{24}/10^{21}$, 10–100 Ma after a load is applied to the lithosphere the system relaxes to a state resembling Airy isostasy [*Watts and Zhong*, 2000]. While there was likely a buried buoyant load related to the vast quantities of volcanism produced in the formation of these features, thermally buoyant support is likely to have cooled to ambient density in the 100 Ma or more since the formation of these features. Additionally, plate motion is likely to have carried these loads away from the asthenospheric material that was under them at the time of formation. Admittance and coherence studies of another Pacific large igneous province, the Ontong Java Plateau similarly show that for long wavelength features either Airy isostasy or a very thin elastic plate is required to support the topography, while for shorter wavelengths more complicated loading histories with both surface and subsurface loads are required to match observations [*Ito and Taira*, 2000].

3.4. Crustal Thickness

[27] The admittance calculations in the previous section have shown that shallow crustal compensation, either through Airy isostasy or plate flexure due to surface loading, accounts for most of the RMBA signal we observe in the northwest Pacific region. The only apparent exception is the Hawaiian swell, which could be alternatively explained as resulting from deep buried loads in the mantle. We therefore estimate crustal thickness variations by converting the RMBA map into a Moho topography map through downward continuation of the gravity anomaly signal to an appropriate depth. It should be emphasized that while we have used various compensation models to evaluate the probable source of observed RMBA gravity anomalies, no specific compensation model goes into the crustal thickness calculation. We simply estimate the amount of excess crust necessary to account for the total observed gravity anomalies. This therefore represents an end-member maximum crustal thickness variation: contributions to the observed RMBA from mantle density variations or buried loads would reduce the fraction of the gravity signal which comes from crustal thickening and make our calculated Moho topography too deep.

[28] The equation for the downward continued Moho topography $M(k)$ in terms of the observed gravity anomaly $B(k)$ is

$$M(k) = -\frac{\exp(kz_{\mathrm{CR}})}{2\pi G(\rho_m - \rho_c)} B(k)C(k), \tag{8}$$

where z_{CR} is the mean crustal root depth below sea level, as in equation (2), and $C(k)$ is a low-pass cosine filter applied to prevent the amplification of short-wavelength noise in the RMBA. All wavelengths larger than λ_{large} are completely preserved in the calculation, all wavelengths smaller than λ_{small} are completely filtered out, and wavelengths between the two are tapered smoothly. In order to choose the best value for the two parameters, we tested many λ_{small} values with a constant offset between λ_{small} and λ_{large} of 20 km. We then tested a variety of offsets for two likely λ_{small} values, 35 km and 75 km (Figure 8). The best values were taken to be the combination of parameters that minimized both the rms relief on the Moho and the rms misfit between the observed gravity anomaly and that predicted by upward continuation, i.e., working backward, from the Moho topography [*Blackman and Forsyth*, 1991]. We choose λ_{large} to be 135 km and λ_{small} to be 35 km, which is consistent with the coherence of satellite gravity signals when compared to shipboard gravity [*Neumann et al.*, 1993].

[29] The resulting Moho topography is converted to a crustal thickness map by subtracting the seafloor bathymetry from the calculated Moho depth (Figure 9). For consistency, we filter the seafloor bathymetry with the same cosine filter that was applied to the Moho topography calculation. The resultant crustal thickness map shows an average thickness of 6 km with 2–4 km of excess crustal thickness along the Hawaiian swell and up to 12 km of excess crustal thickness along the Hawaii-Emperor seamount chain and under Hess Rise. Comparing an interpreted seismic profile across the Hawaiian island of Oahu [*ten Brink and Brocher*, 1987] with our crustal thickness estimation (Figure 10) shows that within 200 km of the island our gravity-derived crust-mantle boundary depth is roughly consistent with the seismically determined Moho. Beyond 200 km distance from Oahu, the Hawaiian swell RMBA leads us to overpredict the crustal thickness compared to the interpreted seismic profile. Note that if part of the observed RMBA over the Hawaiian swell is due to deep buried loads in the mantle as discussed previously, the discrepancy between the remaining RMBA signals and the seismic data would be less. However it is also worth noting that all of the seismic data used to produce *ten Brink and Brocher's* [1987] Oahu crustal structure profile is confined to a distance of 200 km or less from the Oahu island, so they lack constraints on crustal structure under the full width of the Hawaiian swell.

[30] It would be useful to compare our calculated crustal thickness maps for the Mid-Pacific Mountains and Hess and Shatsky Rises with seismic crustal thicknesses. Unfortunately, few seismic surveys or measurements appear to have been made for the Mid-Pacific Mountains. The seismic data that exists for Hess Rise [*Kogan et al.*, 1982; *Kroenke and Nemoto*, 1982; *Vallier et al.*, 1983] is restricted to multichannel reflection profiles of sediment and basement structures that fails to image a Moho reflector, although *Kogan et al.* [1982] do note that the crustal thickness must be at least twice as thick as normal ocean crust. Although modern seismic work on Shatsky Rise appears to be limited to reflection survey for ODP Leg 198 [*Klaus and Sager*, 2002] (see http://www-odp.tamu.edu/publications/198_IR/chap_11/c11_.htm), two older seismic refraction studies exist. *Den et al.* [1969] found that the depth to the mantle was at least 22 km under the crest of the Shatsky Rise and *Gettrust et al.* [1980] concluded that if a Moho discontinuity exists in their data, its depth is greater than 26 km. The greatest crustal thickness we calculated for Shatsky Rise is

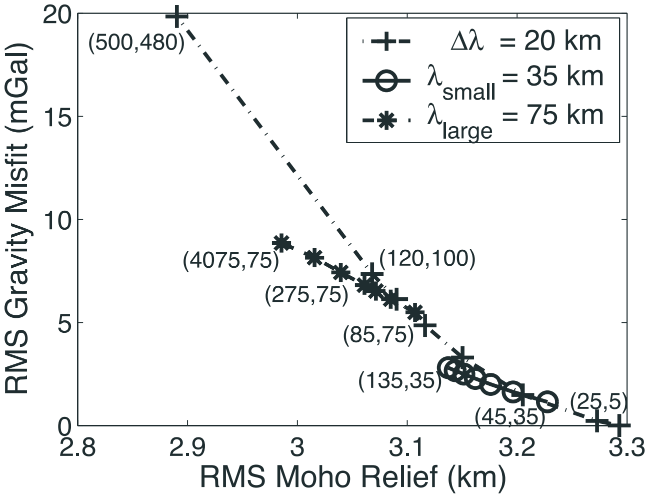

Figure 8. Finding the best filtering wavelengths for the calculation of Moho topography by downward continuation of the RMBA gravity signal. The filter should minimize amplification of short wavelength noise, while introducing minimal misfit between the original observed RMBA and that predicted from upward continuation of the resulting Moho topography. These two goals are measured by the rms Moho relief axis and the rms gravity misfit axis, respectively. Each point represents a downward continuation run with a different combination of (λ_{large}, λ_{small}) cut-off wavelengths, and select points are labeled with the values used for that run. The dash-dotted line shows runs with a constant offset of 25 km between the small and large wavelengths, the dashed line shows runs with a short wavelength cutoff of 75 km and various long wavelength cutoffs, and the solid line shows runs with a short wavelength cutoff of 35 km and various long wavelength cutoffs. We choose a best-fitting combination of (135 km, 35 km), which is consistent with the spatial precision found for marine and satellite gravity anomalies in other studies [*Blackman and Forsyth*, 1991; *Neumann et al.*, 1993].

19 km, a result which is comparable although slightly smaller than those two observations.

3.5. Igneous Volume Flux

[31] Using our crustal thickness map for the northwest Pacific, we can calculate the along-axis profiles of excess crust and the corresponding hot spot igneous volume flux generated by the interaction of the Hawaiian hot spot with the Pacific lithosphere. First we subtract the 6 km reference crust from the crustal thickness map (Figure 9c) to find the excess crustal thickness E(x,y) (Figure 11a). Next we rotate the coordinates from latitude and longitude to x' and y', where y' follows the axis of the Hawaii-Emperor seamount chain (Figure 11b). Finally, we integrate

$$\mathrm{Flux}(y') = v \int_{-hw}^{+hw} E(x', y') dx', \tag{9}$$

where v is the relative speed between the hot spot and the plate and converts a volume per unit distance along-axis to a volume per unit time. "Flux" is therefore an along-axis crustal volume flux (Figure 11c), which we use as a proxy for igneous production flux over time.

[32] In order to capture all of the Hawaii-Emperor seamounts we use a half-width, *hw*, of 200 km. This choice deliberately fails to capture the whole width of the Hawaiian swell because the broad swell could be supported by deep buried loads rather than thickened crust. Using a half-width of 200 km limits the swell contamination to ~10% of the crustal thickness used to calculate the flux (Figure 10). If we take a wider half-width of 600 km, the whole swell would be captured, resulting in slightly higher flux values in the younger parts of the Hawaiian chain, while retaining a similar shape to the flux curve. However, choosing such a greater half-width would lead to some contamination in the Emperor-Hawaii flux calculations due to the unintended inclusion of the Hess Rise and Shatsky Rise signals near the bend between the Emperor and Hawaiian ridges.

[33] For the Hawaiian ridge we use a constant plate velocity, v, of 8.3 cm/yr [*Gordon and Jurdy*, 1986], while for the Emperor seamounts we use a rate of hot spot motion relative to the plate suggested by recent paleomagnetic results. *Tarduno et al.* [2003] produced two estimates of hot spot motion southward during the formation of the Emperor seamounts: 43.1 ± 22.6 mm/yr and 57.7 ± 19.2 mm/yr. We use the larger value as it seems to result in a good correlation between the peaks in the Emperor seamounts section of Figure 11c and the ages of the Koko (49 Ma), Nintoku (56 Ma), and Detroit (75–81 Ma) seamounts summarized in *Tarduno et al.* [2003].

[34] Results of the igneous volume flux calculations show that the hot spot has had a volcanic production rate of near 8 m^3/s (0.25 km^3/yr) in recent times (Figure 11c), although this is probably an underestimation due to the lack of proper gravity data coverage for the Hawaiian islands. The volcanic flux was only 4 m^3/s from 8 to 18 Ma, however it was slightly greater than 8 m^3/s at 20 Ma. For the Emperor ridge, the calculated flux reached two very low flux periods near 55 Ma and 65 Ma (Figure 11c). Furthermore, we note that during the low-flux periods at 25–48, 57, and 75 Ma, the height and size of individual hot spot seamounts also appear to be noticeably less than those of the high-flux periods.

[35] The two previous studies which calculated igneous or volcanic fluxes over the time span of the Hawaii-Emperor chain share certain gross features with our results. *White* [1993] and *Vidal and Bonneville* [2004] both have high magmatic production rates during the Hawaiian chain from 0 to ~25 Ma with a low point within that time span at ~10 Ma, a large decrease in flux around the bend in the chain, and much lower magmatic fluxes during the Emperor chain. The 0 Ma magnitude of the flux is much greater for *Vidal and Bonneville* [2004] than in our study. One of the effects that may contribute to such a discrepancy is underestimation due to the lack of gravity data coverage on the Hawaiian islands in our calculations. The magnitude of the next peak in the igneous volume flux down the chain from the present is similar between our result and *Vidal and Bonneville* [2004] and double that found by *White* [1993]. However that peak is offset in time between our result (~19 Ma) and *Vidal and Bonneville* [2004] (~15 Ma). It is unclear how *Vidal and Bonneville* [2004] converted distance to time along the Hawaiian ridge, which makes it difficult to account for this difference. The largest

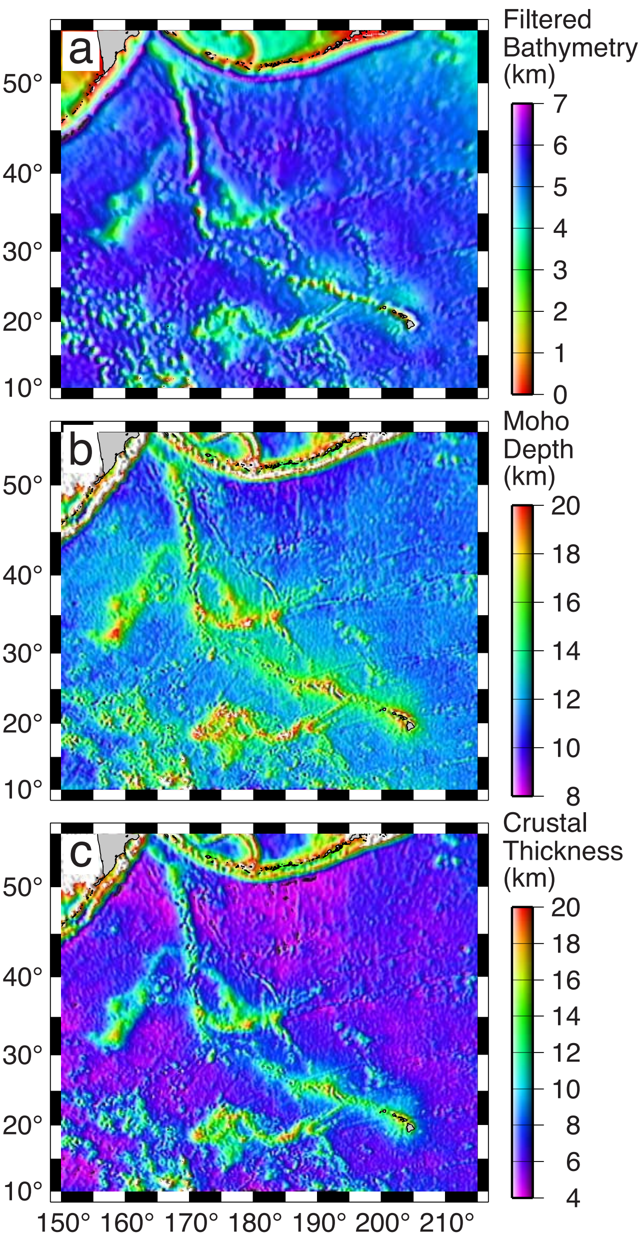

Figure 9. Calculation of crustal thickness. (a) Ship track bathymetry filtered with a cosine taper between λ_{long} = 135 km and λ_{short} = 35 km. (b) The Moho depth below sea level, calculated from downward continuation of the observed RMBA after applying a cosine taper similar to that applied to the bathymetry in Figure 9a. The values shown in Figure 9b are based on the assumption that all the observed RMBA signal is due to excess crustal thickness. (c) Calculated crustal thickness, which is obtained by subtracting the seafloor bathymetry in Figure 9a from the calculated Moho depth in Figure 9b. The crustal thickness map shows an average thickness of 6 km, with 2–4 km of excess crustal thickness along the Hawaiian swell and up to 12 km of excess crustal thickness along the Hawaii-Emperor Seamount chain and under Hess Rise. These results are consistent with the limited seismic reflection and refraction data available around Hawaii [*ten Brink and Brocher*, 1987].

difference between our igneous volume flux and that of the prior studies is found in the Emperor chain, where both prior studies found similar low-flux values (1–2 m^3/s) which remained fairly constant over the length of the chain. In contrast, we have distinct variations in flux between 4 and 0 m^3/s in the Emperor chain on a timescale of 10–20 Ma. This is perhaps due to the finer 10 km along-axis distance steps used in our calculation, as opposed to the 1° along-axis windowing used by *Vidal and Bonneville* [2004].

3.6. Igneous Volume Flux Periods

[36] In order to better quantify the flux variations we observed, the power spectral density of the crustal volume flux, or igneous volume flux (Figure 11c) was calculated

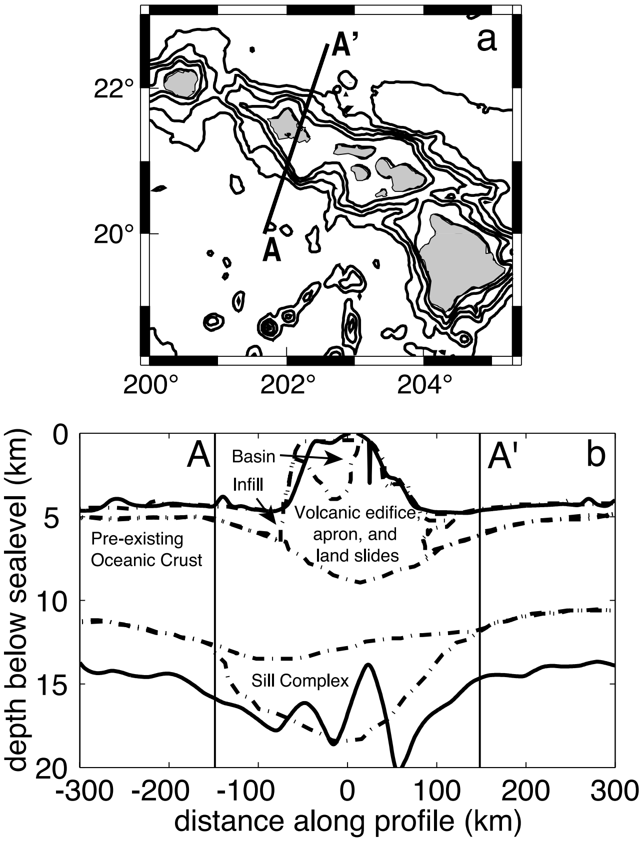

Figure 10. Crustal cross section across the island of Oahu. (a) Ship track bathymetry contoured every 1000 m with the A–A′ profile used by *ten Brink and Brocher* [1987]. (b) Digitized interfaces from the crustal structure of the island of Oahu inferred from reflection and refraction marine seismic profiles collected around the island [*ten Brink and Brocher*, 1987] (dash-dotted lines) are compared with the ship track bathymetry and our gravity-derived crust-mantle interface (solid lines). Our calculated Moho (lower solid line) compares well with the seismic crustal thickness (lowest dash-dotted line) near the seamount. At distances greater than 200 km from Oahu the gravitational signal of the Hawaiian swell leads us to overpredict crustal thickness relative to the seismic interpretation. However, it is worth noting that the seismic interpretation is based on data that is confined between A and A′ and is therefore not well constrained under the swell.

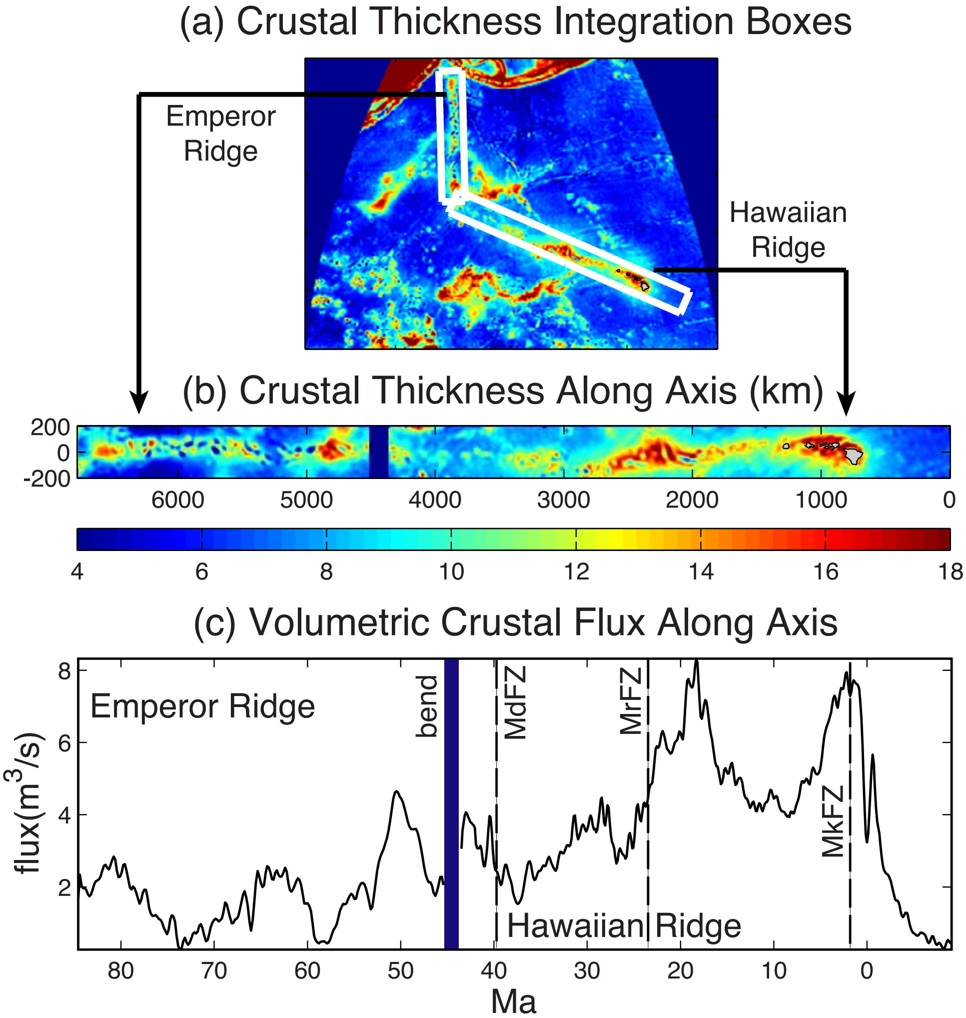

Figure 11. Igneous volume flux calculation. (a) Calculated map of crustal thickness. The cut-out stripes of the Emperor ridge and Hawaiian ridge are shown by white boxes. (b) Crustal thickness stripes cut from Figure 11a and rotated. Data within these stripes are then integrated to find (c) the igneous (crustal) volumetric flux. The half-width of the stripe chosen for the crustal volume flux integration calculations is 200 km, and the along-axis distance is converted to an along-axis age of the Hawaiian chain by assuming a constant plate velocity of 8.3 cm/yr [*Gordon and Jurdy*, 1986] and along-axis age of the Emperor chain using the hot spot plate relative speed of 5.77 cm/yr proposed by *Tarduno et al.* [2003]. The thick blue line shows the location of the bend in the hot spot chain, and the dashed lines show the approximate location of the major Pacific fracture zones (FZ) as inferred from Figure 1: MkFZ, Molokai FZ; MrFZ, Murray FZ; MdFZ, Mendocino FZ.

using a fast Fourier transform convolved with a Hanning filter. The spectra were then smoothed using a moving window that averaged every 10 adjacent frequency bins, reducing the variance of the spectra at the expense of reduced resolution.

[37] The spectral energy in the both the unsmoothed and smoothed power density spectrums of the igneous volume flux (Figure 12) is largest in a range of periods between 6.2 and 30.8 My. This reflects the somewhat irregular spacing of the peaks and troughs of the igneous volume flux in Figure 11c, which varies between 8.3 and 17.4 Ma with an average of 12.8 My and a standard deviation of 3.1 My. The 15.4 My period on the unsmoothed spectrum thus seems to be an average value corresponding to the 8–17 My spacing of peaks and troughs in the flux results. The 30.8 My peak seems to be an average value of the distance between the 20 Ma, 50 Ma, and 80 Ma peaks in Figure 11c. Short wavelength signals have largely been filtered out by the λ_{small} = 135 km value used in the crustal thickness calculation, equivalent to ~1.6 My.

4. Discussion

4.1. Admittance and Flux Implications

[38] The results from the admittance functions for Airy isostasy, plate flexure with surface loading, and plate flexure with buried loading indicate that the relatively narrow Hawaiian hot spot seamounts are probably supported by plate flexure in response to surface loading. While admittance modeling results for the broader Hawaiian hot spot swell are ambiguous, the greater success of the buried load flexure in modeling the shape of the Hawaiian swell leads to

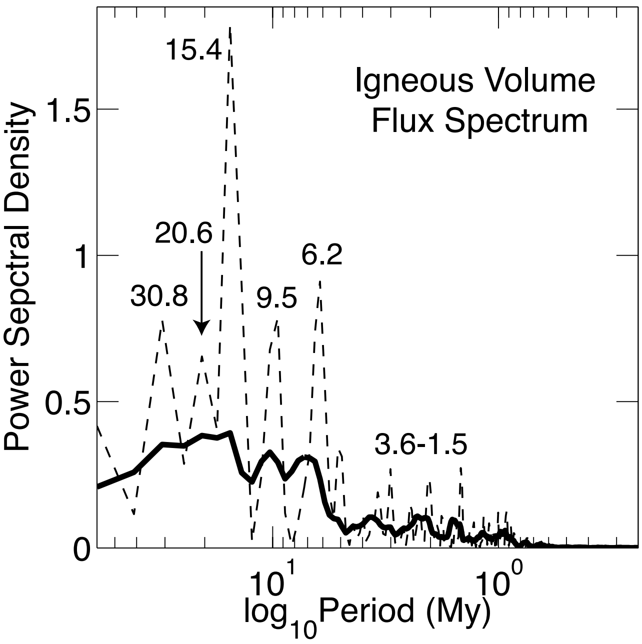

Figure 12. Power spectral density of the igneous volume flux time series shown in Figure 11. The spectra were calculated using a Fourier transform with a Hanning filter. The raw power spectral densities (dashed line) and the 10-bin windowed average of the raw spectrum (thick solid line) are shown.

our preference of the hypothesis that the swell is supported by a buried buoyant load at approximately 120 km depth. The support of the seamounts by plate flexure is not surprising since the theory of elastic plates predicts that short wavelength features should be supported by the plate strength.

[39] Our preferred hypothesis of a buried load supporting the Hawaiian hot spot swell contrasts with the other Pacific long-wavelength bathymetric features, the Hess, Shatsky, and Mid-Pacific igneous plateaus, which seem to be supported by Airy isostasy with a low-density crustal root. There are a few probable explanations for a buried load supporting the swell: a depleted, low-density region caused by the melt extraction from the mantle to supply the Hawaiian hot spot volcanism [*Jordan*, 1979; *Robinson*, 1988; *Phipps Morgan et al.*, 1995] or a warm, low-density region of thermally buoyant material supplied by a plume from deep in the mantle and trapped under the oceanic lithosphere [*Crough*, 1978, 1983; *Detrick and Crough*, 1978; *Davies*, 1988; *Sleep*, 1990], or a combination of both. While we cannot definitively select one of these models, we can speculate that if a buoyant depleted mantle is supporting the swell, the volume of that depleted melting source could be correlated with the amount of excess crustal material which has been erupted as seamounts and underplated the crust. Thus the igneous volume flux might provide some measure of the volume of a depleted, buoyant mantle melting source located under the hot spot track.

4.2. Potential Causes of Flux Variations

[40] We have shown that the igneous volume flux of the Hawaii-Emperor hot spot has varied widely on timescales of 6–30 My with amplitude variations between 0 and 8 m^3/s (Figure 11c). With the igneous volume flux we have measured the end-member crustal production of the hot spot. Are the variations we observe in such hot spot crustal production controlled by variations in the mantle plume supplying the hot spot, the nature of the lithosphere with which the hot spot is interacting, or both?

[41] *Phipps Morgan et al.* [1995] have hypothesized that the variations in Hawaiian volcanic production are due to changes in the overlying lithosphere as the various Pacific fracture zones crossed the stationary mantle source. This hypothesis argues that under the younger, warmer, and thus thinner lithosphere between the Molokai and Murray FZs, hot spot material would ascend higher and melt more than under the older, cooler, and thicker lithosphere between the Murray and Mendocino FZs (Figure 1). While this is a plausible explanation for the Hawaiian ridge portion of the hot spot track, it fails to account for the flux variations we have observed in the Emperor seamount chain, which lacks dramatic fracture zone crossings. This model is also unable to explain the observed reduction in the fluxes at ~10 Ma on the Hawaiian chain, which lies within the "warmer" lithosphere bounded by the Molokai and Murray FZs (Figure 11). However, we note that this low-flux region is geographically close to where the Mid-Pacific Mountains feature (123–132 Ma old) connected to the Hawaiian ridge, although the detailed style of potential interaction between the two volcanic features is not clear at present.

[42] To explain the variations in the Emperor seamount crustal volume fluxes, we turn attention to recent paleomagnetic studies [*Tarduno and Cottrell*, 1997; *Shipboard Scientific Party*, 2002a; *Cottrell and Tarduno*, 2003], which have suggested that the Hawaii-Emperor hot spot was moving south at rates of 30–50 mm/yr during the formation of the Emperor seamounts. It seems possible that the dynamics of the moving hot spot plume conduit during this time period could affect the hot spot flux being supplied under the lithosphere. The detailed kinematics of interactions between a moving plume conduit and the surrounding mantle convection have been investigated by *Steinberger and O'Connell* [1998] and *Steinberger* [2000]. The further expansion of such studies to include flux variations in the plume conduits should be an interesting area for further research.

[43] V-shaped ridges propagating along the Mid-Atlantic Ridge south of the Iceland hot spot were successfully modeled by *Ito* [2001] as the result of hot spot flux variation due to a periodic oscillation in the radius of the hot spot mantle plume conduit. *Ito* [2001] hypothesized that such an oscillation could be caused by the surfacing of solitary waves in the Iceland mantle plume. Solitary waves are stable traveling perturbations in the width of a buoyant, viscous fluid conduit due to perturbations in the flux of the fluid entering the conduit [*Scott et al.*, 1986; *Olson and Christensen*, 1986; *Whitehead*, 1987]. *Sleep* [1992] suggested a possible source of those perturbations in the flux of the fluid entering the conduit due to the dynamics of the evolving boundary layer at the bottom of the mantle. The presence of similar V-shaped anomalies south of the Azores hot spot [*Escartin et al.*, 2001] suggests that such a mechanism may be applicable for other hot spots as well. Because of their close proximity to the mid-ocean spreading

center, the variations in the Azores and Iceland hot spot flux is expressed as changes in crustal thickness along the Mid-Atlantic Ridge [*Escartin et al.*, 2001]. Similarly, it is possible that solitary wave-like variations in the Hawaiian-Emperor hot spot flux might result in crustal thickness variations as reflected in our results (Figures 11 and 12).

[44] One possible way to distinguish between the proposed lithospheric versus plume conduit sources of flux variation would be to examine the geochemistry of the volcanic rocks along the Hawaii-Emperor seamount chain for signals of melting depth variation. *Regelous et al.* [2003] compare MgO/FeO ratios, La/Yb and Lu/Hf ratios, and trace element compositions between Detroit and Meiji tholeiites and other Hawaiian-Emperor tholeiites and conclude that those values vary with the age of the underlying oceanic lithosphere at the time of seamount formation. Likewise, *Keller et al.* [2000] see a correlation between $^{87}Sr/^{86}Sr$ ratios and seamount-crust age difference. However, R. A. Keller et al. (Cretaceous-to-recent record of elevated $^3He/^4He$ along the Hawaiian-Emperor volcanic chain, submitted to *Geochemistry, Geophysics, Geosystems*, 2003) did not find simple correlations between $^3He/^4He$ isotope ratios and the igneous volume flux calculated in our study, and F. A. Frey et al. (Origin of depleted components in lavas related to the Hawaiian hot spot: Evidence from Hf isotope data, submitted to *Geochemistry, Geophysics, Geosystems*, 2003) inject a discussion of a geochemically depleted component in the Hawaiian hot spot source material that may complicate the above interpretations.

5. Conclusions

[45] 1. We have calculated the residual bathymetry and residual mantle Bouguer anomalies (RMBA) of the northwest Pacific region. The interaction of the Hawaii-Emperor hot spot with the Pacific lithosphere has left a large negative RMBA anomaly, suggesting thickened crust, low-density mantle, or both. The width and magnitude of the RMBA anomaly along the hot spot track vary widely, with the 1000-km-wide hot spot swell visible for a few thousand kilometers downstream from the hot spot's present location.

[46] 2. Applying admittance functions for Airy isostasy, elastic plate flexure with surface loading, and elastic plate flexure with buried buoyant loading to the residual bathymetry allows us to discriminate between sources of the observed RMBA. Incorporating our results with previous seismic and flexure studies of the Hawaiian chain, we conclude that the Hawaii and Emperor seamounts are best explained as being supported by surface loading of elastic plates with thicknesses of 60 and 30 km, respectively, and the Hess Rise, Shatsky Rise, and the Mid-Pacific Mountains igneous plateaus are best modeled by Airy isostasy. Our rms misfit results are more ambiguous for the Hawaiian swell. However, the shape of the Hawaiian swell is best modeled by the flexure due to a buried load at approximately 120 km depth.

[47] 3. Since all bathymetric features except possibly the Hawaiian swell seem to be supported by thickened crust, either through Airy isostasy or through plate bending, we downward continue our calculated residual Bouguer anomaly to find the crustal thickness model that best predicts the observed gravity anomaly while filtering out short-wavelength signals. Integrating the crustal anomaly within a narrow stripe of 200 km half-width centered on the hot spot track yields an estimated present-day Hawaiian igneous volume flux of 8 m^3/s, while the flux was only 4 m^3/s during 8–18 Ma and greater than 8 m^3/s at 20 Ma. From 25 to 48 Ma, the igneous volume flux was in a low period with amplitudes as small as 1 m^3/s. The overall calculated igneous volume flux of the Emperor ridge is substantially smaller than that of the Hawaiian ridge with minimums occurring near 57 and 75 Ma. Furthermore, we note that during the low-flux periods at 25–48, 57, and 75 Ma, the height and size of individual hot spot seamounts also appear to be noticeably less than those of high-flux periods.

[48] 4. We hypothesize that the quasi-periodic variations in the hot spot flux along the Hawaiian ridge may be due to changes in the lithospheric age, temperature, and thickness as the hot spot crossed Pacific fracture zones, as well as potential pulsation of the plume source. We also hypothesize that the quasi-periodic variations in the hot spot flux along the Emperor seamount chain may be due to fluctuations in the plume conduit due to its motion through the mantle. Further combined geochemical and geophysical analyses are required to distinguish between these mechanisms. Since the presence and size of the hot spot swell correlates with hot spot crustal flux variations, we suggest that the likely source of the buried buoyant load supporting the Hawaiian swell is melt-depleted, low-density residual mantle.

[49] **Acknowledgments.** E. Van Ark was supported by a National Science Foundation Graduate Research Fellowship, and J. Lin was supported by NSF grant OCE-0129741 and the Andrew W. Mellon Foundation Endowed Fund for Innovative Research at WHOI. This paper has been greatly improved thanks to comments by Associate Editor Don Forsyth, Norm Sleep, and an anonymous reviewer. We are grateful to Jennifer Georgen for much assistance in the early stages of this project and to Garret Ito, Mark Behn, Allegra Hosford, Seth Stein, Bob Detrick, Maria Zuber, Tim Grove, Jack Whitehead, and the WHOI Marine Tectonics and Geodynamics Group for helpful discussions and valuable suggestions. This is Woods Hole Oceanographic Institution contribution 11091.

References

Arnaud-Vanneau, A., and W. V. Sliter (1995), Early Cretaceous shallow-water benthic foraminifers and fecal pellets from Leg 143 compared with coeval faunas from the Pacific Basin, Central America, and the Tethys, *Proc. Ocean Drill. Program Sci. Results*, *143*, 537–564.
Bargar, K. E., and E. D. Jackson (1974), Calculated volumes of individual shield volcanoes along the Hawaiian-Emperor chain, *U. S. Geol. Surv. J. Res.*, *2*, 545–550.
Blackman, D. K., and D. W. Forsyth (1991), Isostatic compensation of tectonic features of the Mid-Atlantic Ridge: 25°–27°30′S, *J. Geophys. Res.*, *96*, 11,741–11,758.
Calmant, S. (1987), The elastic thickness of the lithosphere in the Pacific Ocean, *Earth Planet. Sci. Lett.*, *85*, 277–288.
Cottrell, R. D., and J. A. Tarduno (2003), A Late Cretaceous pole for the Pacific plate: Implications for apparent and true polar wander and the drift of hotspots, *Tectonophysics*, *362*, 321–333.
Crough, S. T. (1978), Thermal origin of mid-plate hot-spot swells, *Geophys. J. R. Astron. Soc.*, *55*, 451–469.
Crough, S. T. (1983), Hotspot swells, *Ann. Rev. Earth Planet. Sci.*, *11*, 165–193.
Davies, G. F. (1988), Ocean bathymetry and mantle convection: 1. Large-scale flow and hotspots, *J. Geophys. Res.*, *93*, 10,467–10,480.
Davies, G. F. (1992), Temporal variation of the Hawaiian plume flux, *Earth Planet. Sci. Lett.*, *113*, 277–286.
Den, N., W. J. Ludwig, S. Murauchi, J. I. Ewing, H. Hotta, N. T. Edgar, T. Yoshii, T. Asanuma, K. Hagiwara, and T. Sato (1969), Seismic-refraction measurements in the northwest Pacific Basin, *J. Geophys. Res.*, *74*, 1421–1434.
Detrick, R. S., and S. T. Crough (1978), Island subsidence, hot spots, and lithospheric thinning, *J. Geophys. Res.*, *83*, 1236–1244.

Divins, D. (2001), Total sediment thickness of the world's oceans & marginal seas, http://www.ngdc.noaa.gov/mgg/sedthick/sedthick.html, Mar. Geol. and Geophys. World Data Cent., Boulder, Colo.

Divins, D. L., and P. D. Rabinowitz (1991), Total sediment thickness map for the South Atlantic Ocean, in *International Geological-Geophysical Atlas of the Pacific Ocean*, edited by G. B. Udintsev, pp. 147–148, Intergovern. Oceanogr. Comm., Paris.

Escartin, J., M. Cannat, G. Pouliquen, A. Rabain, and J. Lin (2001), Crustal thickness of V-shaped ridges south of the Azores: Interaction of the Mid-Atlantic Ridge (36°–39°N) and the Azores hot spot, *J. Geophys. Res.*, *106*, 21,719–21,735.

Georgen, J. E., J. Lin, and H. J. B. Dick (2001), Evidence from gravity anomalies for interactions of the Marion and Bouvet hotspots with the Southwest Indian Ridge: Effects of transform offsets, *Earth Planet. Sci. Lett.*, *187*, 283–300.

Gettrust, J. F., K. Furukawa, and L. W. Kroenke (1980), Crustal structure of the Shatsky Rise from seismic refraction measurements, *J. Geophys. Res.*, *85*, 5411–5415.

Gordon, R. G., and D. M. Jurdy (1986), Cenozoic global plate motions, *J. Geophys. Res.*, *91*, 12,389–12,406.

Hayes, D. E., and J. L. LaBrecque (1991), Sediment isopachs: Circum-Antarctic to 30S, in *Marine Geology and Geophysics Atlas of the Circum-Antarctic to 30S*, edited by D. E. Hayes, pp. 29–33, AGU, Washington, D. C.

Hilde, T. W. C., N. Isezaki, and J. M. Wageman (1976), Mesozoic sea-floor spreading in the North Pacific, in *The Geophysics of the Pacific Ocean Basin and Its Margin*, *Geophys. Monogr. Ser.*, vol. 19, edited by G. H. Sutton, M. H. Manghnani, and R. Moberly, pp. 205–226, AGU, Washington, D. C.

Hoffman, A. W. (1997), Mantle geochemistry: The message from oceanic volcanism, *Nature*, *385*, 219–229.

Ito, G. T. (2001), Reykjanes "V"-shaped ridges originating from a pulsing and dehydrating mantle plume, *Nature*, *411*, 681–684.

Ito, G., and J. Lin (1995), Mantle temperature anomalies along the present and paleoaxes of the Galapagos spreading center as inferred from gravity analyses, *J. Geophys. Res.*, *100*, 3733–3745.

Ito, G., and A. Taira (2000), Compensation of the Ontong Java Plateau by surface and subsurface loading, *J. Geophys. Res.*, *105*, 11,171–11,183. (Correction, *J. Geophys. Res., 105*, 25,873–25,874, 2000.)

Ito, G., J. Lin, and C. W. Gable (1996), Dynamics of mantle flow and melting at a ridge-centered hotspot: Iceland and the Mid-Atlantic Ridge, *Earth Planet. Sci. Lett.*, *144*, 53–74.

Jenkyns, H. C. (1995), Carbon-isotope stratigraphy and paleoceanographic significance of the Lower Cretaceous shallow-water carbonates of Resolution Guyot, Mid-Pacific Mountains, *Proc. Ocean Drill. Program Sci. Results*, *143*, 99–104.

Jenkyns, H. C., C. K. Paull, D. I. Cummins, and P. D. Fullagar (1995), Strontium-isotope stratigraphy of Lower Cretaceous atoll carbonates in the Mid-Pacific Mountains, *Proc. Ocean Drill. Program Sci. Results*, *143*, 89–97.

Jordan, T. H. (1979), Mineralogies, densities and seismic velocities of garnet lherzolites and their geophysical implications, in *The Mantle Sample: Inclusions in Kimberlites and Other Volcanics: Proceedings of the Second International Kimberlite Conference*, vol. 2, edited by F. R. Boyd and H. O. A. Meyer, pp. 1–14, AGU, Washington, D. C.

Keller, R. A., M. R. Fisk, and W. M. White (2000), Isotopic evidence for Late Cretaceous plume-ridge interaction at the Hawaiian hotspot, *Nature*, *405*, 673–676.

King, S. D., J. P. Lowman, and C. W. Gable (2002), Episodic tectonic plate reorganizations driven by mantle convection, *Earth Planet. Sci. Lett.*, *203*, 83–91.

Klaus, A., and W. W. Sager (2002), Data report: High-resolution site survey seismic reflection data for ODP Leg 198 drilling on Shatsky Rise, *Proc. Ocean Drill. Program Initial Rep., Part A*, *198*, 1–21.

Kogan, L. I., L. P. Zonenshayn, and O. A. Schmidt (1982), Structure of the Hess Rise, Pacific Ocean (from data of deep reflection seismic profiles), *Geotectonics*, *16*, 179–189.

Kroenke, L. W., and K. Nemoto (1982), Marine geology of the Hess Rise: 2. Basement morphology, sediment thickness, and structural geology, *J. Geophys. Res.*, *87*, 9259–9278.

Kunze, A. W. G. (1980), On the flexural rigidity and effective viscosity of the lithosphere in the Hawaiian area, *Tectonophysics*, *69*, 1–8.

Kuo, B. Y., and D. W. Forsyth (1988), Gravity anomalies of the ridge-transform system in the South Atlantic between 31° and 34.4°S: Upwelling centers and variations in crustal thickness, *Mar. Geophys. Res.*, *10*, 205–232.

Larson, R. L., and C. G. Chase (1972), Late Mesozoic of the western Pacific Ocean, *Geol. Soc. Am. Bull.*, *83*, 3627–3643.

Li, X., R. Kind, X. Yuan, I. Wolbern, and W. Hanka (2004), Rejuvenation of the lithosphere by the Hawaiian plume, *Nature*, *427*, 827–829.

Lowman, J. P., S. D. King, and C. W. Gable (2003), The role of the heating mode of the mantle in intermittent reorganization of the plate velocity field, *Geophys. J. Int.*, *152*, 455–467.

Mammerickx, J., and G. F. Sharman (1988), Tectonic evolution of the North Pacific during the Cretaceous quiet period, *J. Geophys. Res.*, *93*, 3009–3024.

McNutt, M. K., and A. V. Judge (1990), The superswell and mantle dynamics beneath the South Pacific, *Science*, *248*, 969–975.

McNutt, M., and L. Shure (1986), Estimating the compensation depth of the Hawaiian Swell with linear filters, *J. Geophys. Res.*, *91*, 13,915–13,923.

Montelli, R., G. Nolet, F. A. Dahlen, G. Masters, R. Engdahl, and S.-H. Hung (2004), Finite-frequency tomography reveals a variety of plumes in the mantle, *Science*, *303*, 338–343.

Morgan, W. J. (1971), Convection plumes in the lower mantle, *Nature*, *230*, 42–43.

Muller, R. D., W. R. Roest, J.-Y. Royer, L. M. Gahagan, and J. G. Sclater (1997), Digital isochrons of the world's ocean floor, *J. Geophys. Res.*, *102*, 3211–3214.

Nakanishi, M., K. Tamaki, and K. Kobayashi (1989), Mesozoic magnetic anomaly lineations and seafloor spreading history of the northwestern Pacific, *J. Geophys. Res.*, *94*, 15,437–15,462.

Nakanishi, M., W. W. Sager, and A. Klaus (1999), Magnetic lineations within Shatsky Rise, Northwest Pacific Ocean: Implications for hot spot-triple junction interaction and oceanic plateau formation, *J. Geophys. Res.*, *104*, 7539–7556.

Neumann, G. A., D. W. Forsyth, and D. T. Sandwell (1993), Comparison of marine gravity from shipboard and high-density satellite altimetry along the Mid-Atlantic Ridge, 30.5°–35.5°S, *Geophys. Res. Lett.*, *20*, 1639–1642.

Olson, P., and U. Christensen (1986), Solitary wave propagation in a fluid conduit within a viscous matrix, *J. Geophys. Res.*, *91*, 6367–6374.

Parker, R. L. (1972), The rapid calculation of potential anomalies, *Geophys. J. R. Astron. Soc.*, *31*, 447–455.

Parsons, B., and J. G. Sclater (1977), An analysis of the variation of ocean floor bathymetry and heat flow with age, *J. Geophys. Res.*, *82*, 803–827.

Phipps Morgan, J., W. J. Morgan, and E. Price (1995), Hotspot melting generates both hotspot volcanism and a hotspot swell?, *J. Geophys. Res.*, *10*, 8045–8062.

Pringle, M. S., and G. B. Dalrymple (1993), Geochronological constraints on a possible hot spot origin for Hess Rise and the Wentworth seamount chain, in *The Mesozoic Pacific: Geology, Tectonics, and Volcanism*, *Geophys. Monogr. Ser.*, vol. 77, edited by M. S. Pringle et al., pp. 263–277, AGU, Washington, D. C.

Pringle, M. S., and R. A. Duncan (1995), Radiometric ages of basaltic lavas recovered at sites 865, 866, and 869, *Proc. Ocean Drill. Program Sci. Results*, *143*, 277–283.

Regelous, M., A. W. Hofmann, W. Abouchami, and S. J. G. Galer (2003), Geochemistry of lavas from the Emperor Seamounts, and the geochemical evolution of Hawaiian magmatism from 85 to 42 Ma, *J. Petrol.*, *44*, 113–140.

Ribe, N. M., and U. R. Christensen (1994), Three-dimensional modeling of plume-lithosphere interaction, *J. Geophys. Res.*, *99*, 669–682.

Ribe, N. M., and U. R. Christensen (1999), The dynamical origin of Hawaiian volcanism, *Earth Planet. Sci. Lett.*, *171*, 517–531.

Robinson, E. M. (1988), The topographic and gravitational expression of density anomalies due to melt extraction in the uppermost oceanic mantle, *Earth Planet. Sci. Lett.*, *90*, 221–228.

Sager, W. W., and H. C. Han (1993), Rapid formation of the Shatsky Rise oceanic plateau inferred from its magnetic anomaly, *Nature*, *364*, 610–613.

Sager, W. W., D. W. Handschumacher, T. W. C. Hilde, and D. R. Bracey (1988), Tectonic evolution of the northern Pacific Plate and Pacific-Farallon-Izanagi triple junction in the Late Jurassic and Early Cretaceous (M21–M10), *Tectonophysics*, *155*, 345–364.

Sandwell, D. T. (1982), Thermal isostasy; response of a moving lithosphere to a distributed heat source, *J. Geophys. Res.*, *87*, 1001–1014.

Sandwell, D. T., and W. H. F. Smith (1995), *Marine Gravity from Satellite Altimetry*, Scripps Inst. of Oceanogr., La Jolla, Calif.

Sandwell, D. T., and W. H. F. Smith (1997), Marine gravity anomaly from Geosat and ERS 1 satellite altimetry, *J. Geophys. Res.*, *102*, 10,039–10,054.

Schilling, J.-G. (1991), Fluxes and excess temperatures of mantle plumes inferred from their interaction with migrating mid-ocean ridges, *Nature*, *352*, 397–403.

Scott, D. R., D. J. Stevenson, and J. A. Whitehead (1986), Observations of solitary waves in a viscously deformable pipe, *Nature*, *319*, 759–761.

Sharp, W. D., and D. A. Clague (2002), An older, slower Hawaii-Emperor bend, *Eos Trans. AGU*, *83*(47), Fall Meet. Suppl., Abstract T61C-04.

Shipboard Scientific Party (2002a), Leg 197 summary: Motion of the Hawaiian hotspot, a paleomagnetic test, *Proc. Ocean Drill. Program Initial Rep.*, *197*, 1–92.

Shipboard Scientific Party (2002b), Leg 198 summary: Extreme warmth in the Cretaceous and Paleogene: A depth transect on Shatsky Rise, central Pacific, *Proc. Ocean Drill. Program Initial Rep.*, *198*, 1–148.

Sleep, N. H. (1990), Hotspots and mantle plumes: Some phenomenology, *J. Geophys. Res.*, *95*, 6715–6736.

Sleep, N. H. (1992), Time dependence of mantle plumes: Some simple theory, *J. Geophys. Res.*, *97*, 20,007–20,019.

Smith, W. H. F., and D. T. Sandwell (1994), Bathymetric prediction from dense altimetry and sparse shipboard bathymetry, *J. Geophys. Res.*, *99*, 21,803–21,824.

Smith, W. H. F., and D. T. Sandwell (1997), Global sea floor topography from satellite altimetry and ship depth soundings, *Science*, *277*, 1956–1962.

Stein, C. A., and S. Stein (1992), A model for the global variation in oceanic depth and heat flow with lithospheric age, *Nature*, *359*, 123–129.

Steinberger, B. (2000), Plumes in a convecting mantle: Models and observations for individual hotspots, *J. Geophys. Res.*, *105*, 11,127–11,152.

Steinberger, B., and R. J. O'Connell (1998), Advection of plumes in mantle flow: Implications for hot spot motion, mantle viscosity and plume distribution, *Geophys. J. Int.*, *132*, 412–434.

Tarduno, J. A., and R. D. Cottrell (1997), Paleomagnetic evidence for motion of the Hawaiian hotspot during formation of the Emperor seamounts, *Earth Planet. Sci. Lett.*, *153*, 171–180.

Tarduno, J. A., and W. W. Sager (1995), Polar standstill of the Mid-Cretaceous Pacific plate and its geodynamic implications, *Science*, *269*, 956–959.

Tarduno, J. A., et al. (2003), The Emperor Seamounts: Southward motion of the Hawaiian hotspot plume in Earth's mantle, *Science*, *301*, 1064–1069.

ten Brink, U. S., and T. M. Brocher (1987), Multichannel seismic evidence for a subcrustal intrusive complex under Oahu and a model for Hawaiian volcanism, *J. Geophys. Res.*, *92*, 13,687–13,707.

ten Brink, U. S., and T. M. Brocher (1988), Multichannel seismic evidence for variations in crustal thickness across the Molokai fracture zone in the Mid-Pacific, *J. Geophys. Res.*, *93*, 1119–1130.

Turcotte, D. L., and G. Schubert (2002), *Geodynamics*, 456 pp., Cambridge Univ. Press, New York.

Vallier, T. L., D. K. Rea, W. E. Dean, J. Thiede, and C. G. Adelseck (1981), The geology of Hess Rise, central north Pacific Ocean, *Proc. Ocean Drill. Program Initial Rep.*, *62*, 1031–1072.

Vallier, T. L., W. E. Dean, D. K. Rea, and J. Thiede (1983), Geologic evolution of Hess Rise, central North Pacific Ocean, *Geol. Soc. Am. Bull.*, *94*, 1289–1307.

Vidal, V., and A. Bonneville (2004), Variations of the Hawaiian hot spot activity revealed by variations in the magma production rate, *J. Geophys. Res.*, *109*, B03104, doi:10.1029/2003JB002559.

Walcott, R. I. (1970), Flexure of the lithosphere at Hawaii, *Tectonophysics*, *9*, 435–446.

Watts, A. B. (1976), Gravity and bathymetry in the central Pacific Ocean, *J. Geophys. Res.*, *81*, 1533–1553.

Watts, A. B. (1978), An analysis of isostasy in the world's oceans: 1. Hawaiian-Emperor seamount chain, *J. Geophys. Res.*, *83*, 5989–6004.

Watts, A. B. (2001), *Isostasy and Flexure of the Lithosphere*, 458 pp., Cambridge Univ. Press, New York.

Watts, A. B., and J. R. Cochran (1974), Gravity anomalies and flexure of the lithosphere along the Hawaiian-Emperor seamount chain, *Geophys. J. R. Astron. Soc.*, *38*, 119–141.

Watts, A. B., and S. Zhong (2000), Observations of flexure and the rheology of oceanic lithosphere, *Geophys. J. Int.*, *142*, 855–875.

Watts, A. B., U. S. ten Brink, P. Buhl, and T. M. Brocher (1985), A multichannel seismic study of lithospheric flexure across the Hawaiian-Emperor seamount chain, *Nature*, *315*, 105–111.

White, R. S. (1993), Melt production rates in mantle plumes, *Philos. Trans. Phys. Sci. Eng.*, *342*, 137–153.

Whitehead, J. A. (1987), A laboratory demonstration of solitons using a vertical watery conduit in syrup, *Am. J. Phys.*, *55*, 998–1003.

Wilson, J. T. (1963), A possible origin of the Hawaiian Islands, *Can. J. Phys.*, *41*, 863–870.

J. Lin, Department of Geology and Geophysics, Woods Hole Oceanographic Institution, Woods Hole, MA 02543, USA. (jlin@whoi.edu)

E. Van Ark, MIT-WHOI Joint Program, 77 Massachusetts Avenue, Building 54-517A, Cambridge, MA 02139, USA. (emilyva@mit.edu)